

Title

By
Bradley Stuart Cownden

A Thesis submitted to the Faculty of Graduate Studies of
The University of Manitoba
in partial fulfillment of the requirements for the degree of

Degree

Department of Physics and Astronomy
University of Manitoba
Winnipeg

© 2019 by Bradley Stuart Cownden

Dedication.

Acknowledgments

Abstract

An abstract.

Contents

Acknowledgments	i
Abstract	ii
Table of Contents	iii
1 Introduction	1
2 Nonlinear Evolution of Massive Scalar Fields	2
2.1 Contributions	2
2.2 Introduction	3
2.3 Review	5
2.3.1 Massive scalars, stability, and time scales	5
2.3.2 Methods	7
2.4 Phases	8
2.4.1 Metastable versus unstable phases	9
2.4.2 Behaviors of the irregular phase	11
2.5 Spectral analysis	15
2.5.1 Dependence on mass	16
2.5.2 Spectra of different phases	17
2.5.3 Evolution of spectra	17
2.6 Discussion	20
2.A Convergence Testing	22
3 Perturbative Stability of Massless Scalars in AdS_4	26
3.1 Contributions	26
3.2 Introduction	27
3.3 Minimally Coupled Scalar Fields in AdS_{d+1}	29
3.3.1 Linearized Solutions	29
3.3.2 Two-Time Formalism	30
3.4 Quasi-periodic Solutions in AdS_4	31
3.4.1 Persistence at Large j_{max}	31
3.4.2 High Temperature Perturbations	32
3.4.3 Building High-Temperature Solutions	34
3.4.4 Stability of QP Solutions	35
3.5 Time Evolution of Quasi-Periodic Solutions	36
3.5.1 Quasi-Periodic Solutions	37

3.5.2	High-Temperature Solutions	39
3.6	Discussion	41
3.A	Seeding Methods For Non-Linear Solvers	51
3.B	Auxiliary Integrals For Calculating the T, R, S Coefficients	51
3.C	Frequency of Solution Checking	53
4	Driven, Time-Dependent Operators in Conformal Field Theories	56
4.1	Contributions	56
4.2	Introduction	57
4.3	Massive Scalars in AdS_{d+1}	57
4.4	Discussion	57
4.A	An Appendix	58
	Bibliography	62

List of Figures

2.1	Classes of initial data for massless scalars and initial width σ . Blue dots represent horizon formation; red triangles indicate a lower limit for t_H . Red curves in subfigures 2.1b, 2.1c are $t_H = a\epsilon^{-2} + b$ matched to largest two amplitudes in the curve.	6
2.2	Phase diagram as a function of initial data width σ and scalar mass μ . Filled circles represent the unstable phase, empty circles the stable phase, top-half-filled circles metastability, and right-half-filled circles the irregular phase.	8
2.3	Coefficient a from the fit $t_H = a\epsilon^{-p} + b$ as a function of width σ using $t_{fit} = 60$. Shows data for $\mu = 0$ (green diamonds), 0.5 (red triangles), 1 (yellow stars), 5 (black circles), 10 (cyan squares), 15 (magenta Y), and 20 (blue circles). The orange line is the best power law fit.	9
2.4	Metastable behavior: blue dots represent horizon formation and red triangles a lower limit on t_H . Magenta curves are fits $t_H = a\epsilon^{-p} + b$ over the shown range of amplitudes. See table 2.1 for best fit parameters.	10
2.5	Irregular behavior: blue dots represent horizon formation and red triangles a lower limit on t_H	12
2.6	Left: The upper envelope of the Ricci scalar for amplitudes $\epsilon_1 = 3.50$ (blue circles), $\epsilon_2 = 3.51$ (red triangles), and $\epsilon_3 = 3.52$ (green squares) for $\mu = 5, \sigma = 0.34$. Right: $\log(\Delta_{12})$ and best fit (blue circles and line) and $\log(\Delta_{23})$ and best fit (red squares and line), calculated as a function of the midpoint t_{mid} of the time interval.	13
2.7	Radial derivative of the mass function at the indicated time for two chaotic systems. Note the appearance of a secondary wave on top of the main pulse. (μ, σ, ϵ) as indicated.	15
2.8	Left: Spectra of the best fit gaussians (2.7) to the $j = 0$ eigenmode for masses $\mu = 0$ (blue circles), 0.5 (yellow squares), 1 (empty orange circles), 5 (green diamonds), 10 (empty cyan squares), 15 (upward red triangles), and 20 (downward purple triangles). Right: an overlay of the best fit Gaussian and e_0 eigenmode for $\mu = 0$ (solid blue is best fit, orange dashed is eigenmode) and $\mu = 20$ (solid green, red short dashes). . .	16
2.9	Initial ($t = 0$) energy spectra for the indicated evolutions. In order, these represent stable, unstable, metastable, monotonic irregular, non-monotonic irregular, and chaotic irregular initial data.	17
2.10	The time dependence of the energy spectra as a fraction of the total ADM mass for the indicated μ, σ, ϵ . Lower panels show the lowest 7 modes (in colors cyan, red, purple, green, yellow, brown, and gray respectively). Upper panels show cumulative energy to mode $j = 0, 1, 2, 4, 8, 16, 32$ (in colors blue, orange, brown, yellow, aqua, red, and magenta).	18
2.11	Spectra at time $t \approx 71$ for $\mu = 0, \sigma = 1.1$ for the two amplitudes given. $\epsilon = 1.01$ forms a horizon at $t_H \approx 71.1$, $\epsilon = 1.02$ at $t_H \approx 248.0$	19

2.A.1	Convergence results for $\mu = 0.5$, $\sigma = 1$, $\epsilon = 1.12$ showing order of convergence Q vs time for ϕ, M, A, δ (blue, green, red, yellow respectively). Left: Resolutions $n = 14, 15, 16$ used. Right: Resolutions $n = 11, 12, 13$ used.	22
2.A.2	Convergence results for $\mu = 15$, $\sigma = 0.2$. Left: t_H vs ϵ . Middle & Right: order of convergence vs time for ϕ, M, A, δ (blue, green, red, yellow respectively) for indicated amplitudes.	23
2.A.3	Convergence results for $\mu = 0$, $\sigma = 1.1$ for listed amplitudes showing order of convergence Q vs time for ϕ, M, A, δ (blue, green, red, yellow respectively); resolutions $n = 12, 13, 14$	23
2.A.4	Convergence results for $\mu = 1$, $\sigma = 1$. Left: t_H vs ϵ . Middle & Right: order of convergence Q vs time for ϕ, M, A, δ (blue, green, red, yellow respectively); resolutions $n = 11, 12, 13$	24
2.A.5	Order of convergence vs time for ϕ, M, A, δ (red, blue, green, magenta) for $\mu = 20$, $\sigma = 0.19$ and indicated amplitudes.	24
3.1	Energy spectra for various QP solutions.	32
3.2	The results of projecting a $j_{max} = 50$, $\alpha_1 = 0.44$ solution back to the QP plane at various frequencies during high temperature perturbations. Colour changes indicate that the non-linear solver has been applied.	34
3.3	Comparing energy spectra of high-temperature perturbations of an $\alpha_1 = 0.44$ QP solution that have been projected back to the QP plane at different frequencies. . .	36
3.4	Constructing high temperature solutions “by hand.”	37
3.5	Comparing the upper envelope of Π^2 at the origin per light-crossing time for selected low- and high-temperature solutions with $\epsilon = 1$: $j_{max} = 375$, QP $T \simeq 3.15$ (blue crosses); $j_{max} = 75$, high-temperature $T \simeq 26.9$ (yellow octagons); $j_{max} = 100$, high temperature $T \simeq 75.35$ (green squares); $j_{max} = 95$, high temperature $T \simeq 66.6$ (red diamonds).	38
3.6	Residuals from evaluating the constraints for QP and high temperature solutions. .	39
3.7	Amplitude-phase evolution of an $\alpha_1 = 0.2$, $j_{max} = 100$, QP solution with $\epsilon = 0.01$. Similar behaviour is observed for higher j_{max} solutions and over values of $0.2 \leq \alpha_1 \leq 0.44$	40
3.8	<i>Left</i> : L^2 -norm of the residuals of (3.19) evaluated at intervals of 0.025 during the evolution of a $j_{max} = 100$, $\alpha_1 = 0.44$ QP solution with $\epsilon = 0.1$. <i>Right</i> : The spectra of the QP solution at the beginning and end of the evolution.	40
3.9	Intermediate values from the amplitude/phase evolution of a solution are used as seeds for the nonlinear solver at various times. Arrows are oriented from amplitude/phase seed values (circles) to QP plane projections (pentagons).	41
3.10	The evolution of the padded QP solution for $\alpha_1 = 0.2$ and $j_{max} = 200$, with amplitude $\epsilon = 0.1$	42
3.11	<i>Left</i> : Normalized spectra for a $j_{max} = 100$, QP solution that has been padded with five extra modes, then evolved in time. Intermediate spectra are used as seeds for projecting back to the QP plane at times $\tau \simeq 4.1 \times 10^{-3}, 4.1 \times 10^{-2}, 4.1 \times 10^{-1}$ (green, blue, yellow). Arrows are oriented from seed spectra to best fit spectra. <i>Right</i> : Corresponding L^2 -norms of the error for each solution.	43

3.12	<i>Above:</i> The evolution the fraction of the total energy in specific modes for a $T \sim 5.4$, threshold temperature solution for $\tau \in [0, 4.25]$. <i>Below:</i> Snapshots of the full spectrum at various times in its evolution, as well as the upper envelope of $ \mathcal{R}(t, x = 0) $ when $\epsilon = 0.1$	44
3.13	The evolution of a high-temperature solution created by hand from lower j_{max} solutions.	44
3.14	Padding the same initial solution from figure 3.4, but with only 25 extra modes.	45
3.15	Padding a $j_{max} = 100$, high temperature solution to $j_{max} = 200$ and evolving in time. $\epsilon = 0.1$	45
3.16	A high-temperature solution is padded with 25 extra modes, then evolved in time. Above are the results of projecting back to the QP plane at $t \simeq 0.002, 0.004, 0.006, 0.06$ (red diamond, green cross, blue square, yellow triangle, magenta circle).	46
3.17	The evolution of an intermediate, high-temperature solution that <i>does not</i> correspond to a solution of the QP equations.	47
3.18	Padding a threshold temperature solution	48
3.19	Despite the spectrum of the padded threshold temperature solution (figure 3.18) resembling that of lower-temperature QP solutions, these solutions move away from the QP plane and can no longer be projected back.	49
3.20	<i>Top:</i> Overlay of the known threshold temperature solution for $j_{max} = 200$ (thick red line) with snapshots of the spectra of a $j_{max} = 100$ threshold solution that has been padded with zeros to $j_{max} = 200$ after amplitude/phase evolutions of $\tau = 1, 2, 3, 4, 5 \times 10^{-5}$ (blue, green, yellow, magenta, cyan). <i>Bottom:</i> The absolute value of the difference between the cumulative sums of the $j_{max} = 200$ threshold temperature solution and each snapshot spectrum (same colouring).	50
3.A.1	A comparison of seeds predicted by (3.27) to known QP solution. Also included for comparison are the results of fitting the QP solutions to a generic exponential fit.	53
3.A.2	The process and result of tail fitting the α_j spectra of QP solutions to generate better seed values.	54
3.C.1	<i>Left:</i> the result of unchecked perturbations of a $j_{max} = 50$ QP solution up to an intermediate temperature before switching to regular checking. <i>Right:</i> the same procedure is applied to a $j_{max} = 150$ QP solution.	55

List of Tables

2.1	Best fit parameters for the cases shown in figure 2.4 restricting to $t_H > t_{fit} = 60$ and as noted. Values in parentheses are standard errors in the last digit. $\chi^2/\text{d.o.f.}$ is the reduced χ^2 value used as a measure of goodness-of-fit.	11
2.2	Best fit Lyapunov coefficients λ for adjacent amplitude pairs and average λ value for each μ, σ system studied. The parenthetical value is the error in the last digit. . . .	14
3.1	Values of the threshold temperature T_{th} for QP solutions with given j_{max} . Also included is the number of iterations applied (projecting back to the solution plane after every five iterations).	35
3.A.1	α_{50} values for various j_{max} QP solutions.	52

1 Introduction

The introduction.

2 Nonlinear Evolution of Massive Scalar Fields

Published to the arXiv, submitted to Phys Rev D.

2.1 Contributions

What my contributions were

Phase Diagram of Stability for Massive Scalars in Anti-de Sitter Spacetime

[arXiv:1711.00454](https://arxiv.org/abs/1711.00454)

Brad Cownden¹, Nils Deppe², and Andrew R. Frey^{3,4}

¹*Department of Physics & Astronomy,
University of Manitoba
Winnipeg, Manitoba R3T 2N2, Canada
cowndenb@myumanitoba.ca*

²*Cornell Center for Astrophysics and Planetary Science and Department of Physics,
Cornell University
122 Sciences Drive, Ithaca, New York 14853, USA
nd357@cornell.edu*

³*Department of Physics & Astronomy,
University of Manitoba
Winnipeg, Manitoba R3T 2N2, Canada*

⁴*Department of Physics and Winnipeg Institute for Theoretical Physics,
University of Winnipeg
515 Portage Avenue, Winnipeg, Manitoba R3B 2E9, Canada
a.frey@uwinnipeg.ca*

We present the phase diagram of stability of 5-dimensional anti-de Sitter spacetime against horizon formation in the gravitational collapse of a scalar field, treating the scalar field mass and width of initial data as free parameters. We find that the stable phase becomes larger and shifts to smaller widths as the field mass increases. In addition to classifying initial data as stable or unstable, we identify two other phases based on nonperturbative behavior. The metastable phase forms a horizon over longer time scales than suggested by the lowest order perturbation theory, and the irregular phase can exhibit non-monotonic and chaotic behavior in the horizon formation times. Our results include evidence for chaotic behavior even in the collapse of a massless scalar field.

2.2 Introduction

Through the anti-de Sitter spacetime (AdS)/conformal field theory (CFT) correspondence, string theory on $\text{AdS}_5 \times X^5$ is dual to a large N conformal field theory in four spacetime dimensions ($\mathbb{R} \times S^3$ when considering global AdS_5). The simplest time-dependent system to study in this context is the gravitational dynamics of a real scalar field with spherical symmetry, corresponding to the time dependence of the expectation value of the zero mode of a single trace operator in the gauge theory. Starting with the pioneering work of [1–4], numerical studies have suggested that these dynamics may in fact be generically unstable toward formation of (asymptotically) AdS_{d+1} black holes even for arbitrarily small amplitudes. While perhaps surprising compared to intuition from gravitational collapse in asymptotically flat spacetimes, the dual picture of thermalization of

small energies in a compact space is more expected. In terms of the scalar eigenmodes on a fixed AdS background, the instability is a cascade of energy to higher frequency modes and shorter length scales (weak turbulence), which eventually concentrates energy within its Schwarzschild radius. In a naive perturbation theory, this is evident through secular growth terms.

However, some initial scalar field profiles lead to quasi-periodic evolution (at least on the time scales accessible via numerical studies) at small but finite amplitudes; even early work [1, 5] noted that it is possible to remove the secular growth terms in the evolution of a single perturbative eigenmode. A more sophisticated perturbation theory [6–17] supports a broader class of quasi-periodic solutions that can contain non-negligible contributions from many modes, and other stable solutions orbit the basic quasi-periodic solutions [14]. Stable solutions exhibit inverse cascades of energy from higher frequency to lower frequency modes due to conservation laws following from the high symmetry of AdS (integrability of the dual CFT). Stable behavior also appears in the full non-perturbative dynamics for initial profiles with widths near the AdS length scale [18–20]; however, analyses of the perturbative and full dynamics in the literature have not always been in agreement at fixed small amplitudes. For example, some perturbatively stable evolutions at finite amplitude actually form black holes in numerical evaluation of the full dynamics [6, 21, 22]. Understanding the breakdown of the approximations used in the perturbative theory, as well as its region of validity, is an active and important area of research [23–27].

Ultimately, the main goal of this line of inquiry is to determine whether stability or instability to black hole formation (or both) is generic on the space of initial data, so the extent of the “islands of stability” around single-mode or other quasi-periodic solutions and how it varies with parameters of the physics on AdS are key questions of interest. The biggest changes occur in theories with a mass gap in the black hole spectrum, such as AdS_3 and Einstein-Gauss-Bonnet gravity in AdS_5 , which cannot form horizons at small amplitudes. While small-amplitude evolution in AdS_3 appears to be quasi-periodic [28, 29], there is some evidence to point toward late-time formation of a naked singularity in AdS_5 Einstein-Gauss-Bonnet gravity [30, 31] (along with a power law energy spectrum similar to that at horizon formation). Charged scalar and gauge field matter [32] also introduces a qualitative change in that initial data may lead to stable evolution or instability toward either Reissner-Nordström black holes or black holes with scalar hair.

In this paper, we extend the study of massive scalar matter initiated in [33, 34]. Specifically, using numerical evolution of the full gravitational dynamics, we draw the phase diagram of gravitational collapse as a function of scalar field mass and initial scalar profile width. By considering the time to horizon formation as a function of the initial profile’s amplitude, we identify several different classes of stable behavior and indicate them on the phase diagram. Finally, we analyze and characterize these different stable behaviors. Throughout, we work in AdS_5 , due to its relevance to strongly coupled gauge theories in four dimensions and because previous literature has indicated massless scalars lead to greater instability than in AdS_4 (the main other case considered), which makes the effects of the scalar field mass more visible.

We note briefly two caveats for the reader. First, horizon formation always takes an infinite amount of time on the AdS conformal boundary due to the usual time dilation effects associated with horizons; this agrees with the understanding of thermalization in the CFT as an asymptotic process. Horizon formation times discussed in this paper correspond to an approximate notion of horizon formation that we will describe below, but alternate measures of thermalization may be of interest. Second, the black holes we discuss are smeared on the compact X^5 dimensions of the gravitational side of the duality, as in most of the literature concerning stability of AdS, and we are particularly interested in small initial amplitudes that lead to black holes small compared

to the AdS scale. As described in [35–37], small black holes in this situation suffer a Gregory-Laflamme-like instability toward localization on X^5 (which may in fact lead to formation of a naked singularity). At the same time, certain light stable solutions for charged scalars (boson stars) are stable against localization on X^5 [38]. We therefore provisionally assume that the onset of the Gregory-Laflamme-like instability occurs only at horizon formation, not at any point of the earlier horizon-free evolution.

The plan of this paper is as follows: in section 2.3, we review the time scales associated with horizon formation with an emphasis on the behavior of massive scalars and briefly discuss our methods. Then, in section 2.4, we present the phase diagram of different stability behaviors, and an attempt at heuristic analytic understanding appears in 2.5. We close with a discussion of our results.

2.3 Review

In this section, we review results on the stability of scalar field initial data as well as our methods (following the discussion of [34]).

2.3.1 Massive scalars, stability, and time scales

As in most of the literature, we work in Schwarzschild-like coordinates, which have the line element (in asymptotic AdS_{d+1})

$$ds^2 = \frac{1}{\cos^2(x)} \left(-Ae^{-2\delta} dt^2 + A^{-1} dx^2 + \sin^2(x) d\Omega^{d-1} \right) \quad (2.1)$$

in units of the AdS scale. In these coordinates, a horizon appears at $A(x, t) = 0$, but reaching zero takes an infinite amount of time (measured either in proper time at the origin or in conformal boundary time); following the standard approach, we define a horizon as having formed at the earliest spacetime point (as measured by t) where A drops below a specified threshold defined in §2.3.2 below. Of course, horizon formation represents a coarse-grained description since the pure initial state of the dual CFT cannot actually thermalize; a more precise indicator of approximate thermalization may be the appearance of a power law energy spectrum (exponentially cut off) in the perturbative scalar eigenmodes. This indicator is tightly associated with horizon formation (though see [30, 31] for some counterexamples).

A key feature of any perturbative formulation of the gravitational collapse is that deviations from $A = 1, \delta = 0$ appear at order ϵ^2 , where ϵ is the amplitude of initial data. As a result, horizons can form only after a time $t \sim \epsilon^{-2}$; in the multiscale perturbation theory of [6, 7, 9–11, 13–17], there is in fact a scaling symmetry $\epsilon \rightarrow \epsilon', t \rightarrow t(\epsilon/\epsilon')^2$ that enforces the proportionality $t_H \propto \epsilon^{-2}$, where t_H is the (approximate) horizon formation time for unstable initial data at small amplitude.

As a result, initial data can be divided into several classes with respect to behavior at low amplitudes, as illustrated in figure 2.1 for massless scalars. *Stable* initial data evolves indefinitely without forming a horizon. In practice, we identify this type of behavior in numerical evolutions by noting rapid horizon formation at high amplitude with a vertical asymptote in t_H just above some critical amplitude. In our numerical results, we see a sudden jump at the critical amplitude to evolutions with no horizon formation to a large time t_{lim} , possibly with a small window of amplitudes with large t_H just above the critical amplitude. In a few cases, we have captured a greater portion

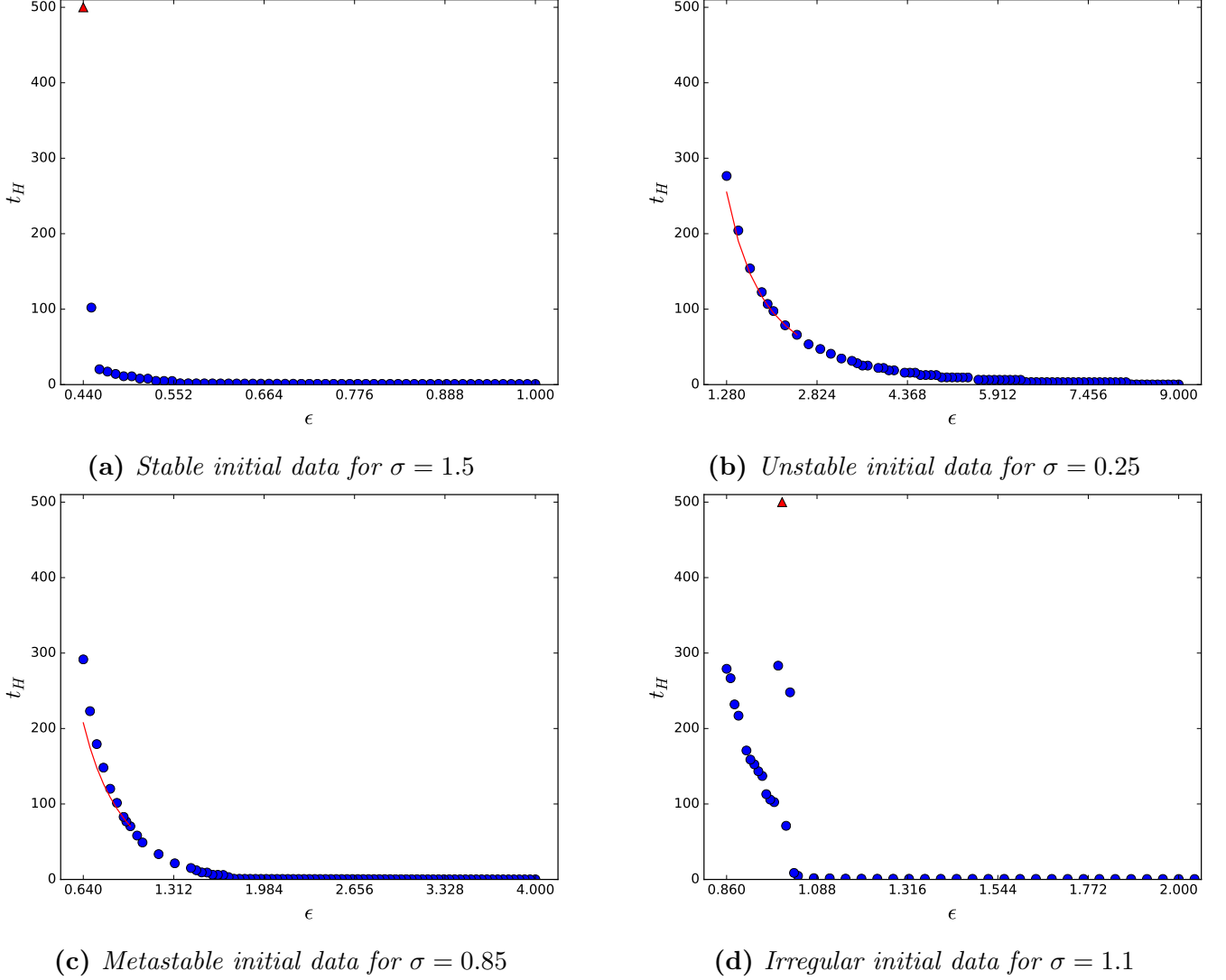


Figure 2.1: Classes of initial data for massless scalars and initial width σ . Blue dots represent horizon formation; red triangles indicate a lower limit for t_H . Red curves in subfigures 2.1b, 2.1c are $t_H = a\epsilon^{-2} + b$ matched to largest two amplitudes in the curve.

of the asymptotic region. See figure 2.1a. *Unstable* initial data, in contrast, forms a horizon at all amplitudes following the perturbative scaling relation $t_H \propto \epsilon^{-2}$ as $\epsilon \rightarrow 0$. In our analysis, we will verify this scaling by fitting t_H to a power law as described in section 2.3.2 below; if we limit the fit to smaller values of ϵ , the scaling becomes more accurate. Figure 2.1b shows unstable data. The red curve is of the form $t_H = a\epsilon^{-2} + b$ with a, b determined by matching the curve to the data for the largest two amplitudes with $t_H \geq 60$ (not a best fit); note that the data roughly follows this curve. The categorization of different initial data profiles with similar characteristic widths into stable and unstable is robust for massless and massive scalars [34]; small and large width initial data are unstable, while intermediate widths are stable. One of the major results of this paper is determining how the widths of initial data in these “islands of stability” vary with scalar mass.

A priori, there are other possible types of behavior, at least beyond the first subleading order in perturbation theory. *Metastable* initial data collapses with $t_H \propto \epsilon^{-p}$ with $p > 2$ at small amplitudes

(or another more rapid growth of t_H as $\epsilon \rightarrow 0$). We will find this type of behavior common on the “shoreline” of islands of stability where stable behavior transitions to unstable. As we will discuss further below, metastable behavior may or may not continue as $\epsilon \rightarrow 0$; in principle, as higher order terms in perturbation theory become less important, the behavior may shift to either stable or unstable as described above. We in fact find circumstantial evidence in favor of the different possibilities. Figure 2.1c shows metastable initial data that continues to collapse to times $t_H \sim 0.6t_{lim}$ but more slowly than ϵ^{-2} ; note that t_H for collapsed evolutions at small amplitudes lies significantly above the curve $t_H = a\epsilon^{-2} + b$ (which is determined as in figure 2.1b). There was one additional type of behavior identified by [34], which was called “quasi-stable” initial data at the time since the low-amplitude behavior was not yet clear. We find here that these initial data are typically stable at small amplitude but exhibit irregular, often strongly non-monotonic or even chaotic, behavior in t_H as a function of ϵ , so we will denote them as *irregular* initial data. Figure 2.1d shows an example of irregular initial data. Later, we will see more striking examples of this behavior for massive scalars.

2.3.2 Methods

For spherically symmetric motion, the Klein-Gordon equation for scalar mass μ can be written in first order form as

$$\phi_{,t} = Ae^{-\delta}\Pi, \quad \Phi_{,t} = (Ae^{-\delta}\Pi)_{,x}, \quad (2.2)$$

$$\Pi_{,t} = \frac{(Ae^{-\delta}\tan^{d-1}(x)\Phi)_{,x}}{\tan^{d-1}(x)} - \frac{e^{-\delta}\mu^2\phi}{\cos^2(x)}, \quad (2.3)$$

where Π is the canonical momentum and $\Phi = \phi_{,x}$ is an auxiliary variable. The Einstein equation reduces to constraints, which can be written as

$$\delta_{,x} = -\sin(x)\cos(x)(\Pi^2 + \Phi^2) \quad (2.4)$$

$$M_{,x} = (\tan(x))^{d-1} \left[A \frac{(\Pi^2 + \Phi^2)}{2} + \frac{\mu^2\phi^2}{2\cos^2(x)} \right], \quad (2.5)$$

$$A = 1 - 2 \frac{\sin^2(x)}{(d-1)\tan^d(x)} M, \quad (2.6)$$

where the mass function M asymptotes to the conserved ADM mass at the boundary $x = \pi/2$. We will restrict to $d = 4$ spatial dimensions. Since results are robust against changes in the type of initial data [34], we can take the initial data to be a Gaussian of the areal radius in the canonical momentum and trivial in the field. Specifically,

$$\Pi(t=0, x) = \epsilon \exp\left(-\frac{\tan^2(x)}{\sigma^2}\right), \quad \phi(t=0, x) = 0. \quad (2.7)$$

The width σ and field mass μ constitute the parameter space for our phase diagram.

We solve the Klein-Gordon evolution equations (2.2,2.3) and Einstein constraint equations (2.4,2.5) numerically using methods similar to those of [20] on a spatial grid of $2^n + 1$ grid points; we discuss the convergence properties of our code in the appendix. We denote the approximate horizon position x_H and formation time t_H by the first point such that $A(x_H, t_H) \leq 2^{7-n}$. In

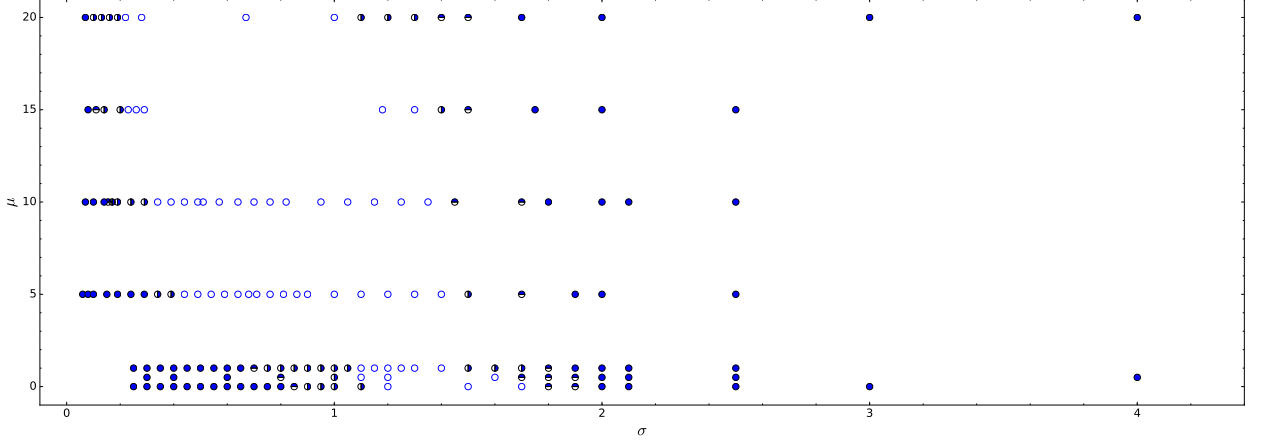


Figure 2.2: Phase diagram as a function of initial data width σ and scalar mass μ . Filled circles represent the unstable phase, empty circles the stable phase, top-half-filled circles metastability, and right-half-filled circles the irregular phase.

detail, we evolve the system in time using a 4th-order Runge-Kutta stepper and initially use a 4th-order Runge-Kutta spatial integrator at resolution $n = 14$. If necessary, we switch to a 5th-order Dormand-Prince spatial integrator and increase resolution near horizon formation. Due to time constraints, we do not increase the resolution beyond $n = 21$ for any particular calculation; if a higher resolution would be required to track horizon formation for a given amplitude, we exclude that amplitude.

To determine the stability class of initial data with a given width σ , we allow evolutions to run to a maximum time of $t_{lim} = 500$ in AdS units, so t_{lim} is a lower limit for t_H for amplitudes that do not form a horizon within that time. Normally, however, if the initial data appears unstable, we only evolve amplitudes with $t_H \lesssim 0.6t_{lim}$; this is partly to save computational resources and partly to distinguish stable evolutions from collapsing ones. For unstable or metastable initial data, we find the best fit of the form $t_H = a\epsilon^{-p} + b$ to evolutions with $t_H > t_{fit}$, where t_{fit} is a constant time chosen such that amplitudes with evolutions that last longer are usually roughly perturbative; in practice, $t_{fit} = 60$ gives results close to the perturbative result $p = 2$ for evolutions expected to be unstable from the literature, but we will also consider $t_{fit} = 80, 100$ as described below.

2.4 Phases

Here we give our main result, the phase diagram of stability classes as a function of initial profile width and scalar mass, along with a more detailed discussion of the scaling of horizon formation time with amplitude for varying initial data.

The stability phase diagram for spherically symmetric scalar field collapse in AdS_5 , treating the width σ of initial data and scalar field mass μ as tunable parameters, appears in figure 2.2. Each (μ, σ) combination that we evolved numerically is indicated by a circle, with filled and empty circles representing the unstable and stable phases respectively. The metastable phase is represented by circles filled in the top half, while the irregular phase are filled in the right half. At a glance, two features of the phase diagram are apparent: as μ increases, the island of stability moves toward smaller values of σ and takes up a gradually larger range of σ . To be specific, the stable phase is

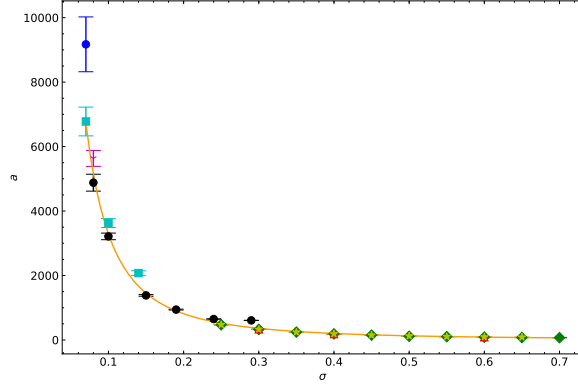


Figure 2.3: Coefficient a from the fit $t_H = a\epsilon^{-p} + b$ as a function of width σ using $t_{fit} = 60$. Shows data for $\mu = 0$ (green diamonds), 0.5 (red triangles), 1 (yellow stars), 5 (black circles), 10 (cyan squares), 15 (magenta Y), and 20 (blue circles). The orange line is the best power law fit.

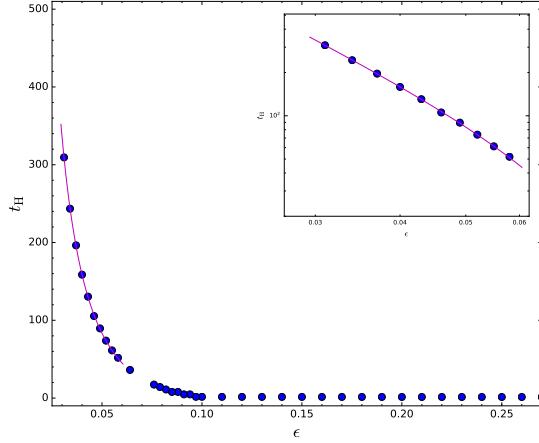
centered at $\sigma = \bar{\sigma} \sim 1.4$ and has a width of $\Delta\sigma \sim 0.7$ for $\mu = 0, 0.5$, with $\bar{\sigma} \sim 1.2$ for $\mu = 1$. $\Delta\sigma$ increases to ~ 1.1 , and the island of stability is centered at $\bar{\sigma} \sim 0.9$ for $\mu = 5, 10$, while $\Delta\sigma \sim 1.2$ for $\mu = 15, 20$ with the stable phase centered at $\bar{\sigma} \sim 0.8$. Note that the transition between “light field” and “heavy field” behavior occurs for $\mu > 1$ in AdS units.

The metastable and irregular phases appear at the shorelines of the island of stability, the boundary between unstable and stable phases. In particular, the slope of the power law $t_H \sim \epsilon^{-p}$ as $\epsilon \rightarrow 0$ increases as the width moves toward the island of stability, leading to a metastable phase. We find metastability at the large σ shoreline for all μ values considered and also at the small σ shoreline for several scalar masses. It seems likely that metastable behavior appears in only a narrow range of σ for larger μ , which makes it harder to detect in a numerical search, leading to its absence in some parts of the phase diagram. We find the irregular phase at the small σ shoreline for every mass and at the large σ boundary for large μ , closer to stable values of σ than the metastable phase. This phase includes a variety of irregular and non-monotonic behavior, as detailed below. Truly chaotic behavior especially becomes more prominent at larger values of μ , as we will discuss below.

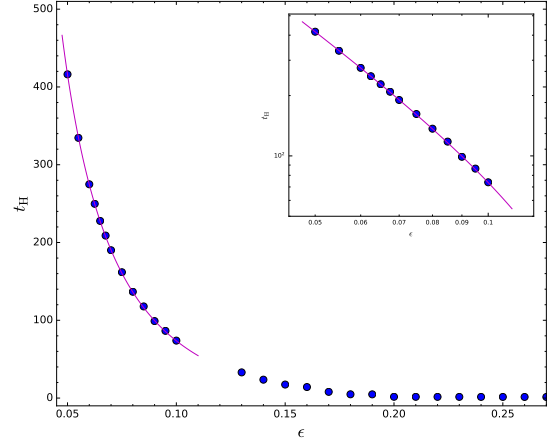
2.4.1 Metastable versus unstable phases

While the stable and irregular phases are typically apparent by eye in a plot of t_H vs ϵ , distinguishing the unstable from metastable phase is a quantitative task. As we described in section 2.3.2, we find the least squares fit of $t_H = a\epsilon^{-p} + b$ to all evolutions with $t_H > t_{fit}$ for the given (μ, σ) , running over values $t_{fit} = 60, 80, 100$. Using the covariance matrix of the fit, we also find the standard error for each fit parameter. We classify a width as having unstable evolution if the best fit value of p is within two standard errors of $p = 2$ for $t_{fit} = 60, 80$ or one standard error for $t_{fit} = 100$ (due to a smaller number of data points, the standard errors for $t_{fit} = 100$ tend to be considerably larger).¹ Considering larger values of t_{fit} helps to ensure that the particular initial profile does not reach the perturbative regime at smaller amplitude values.

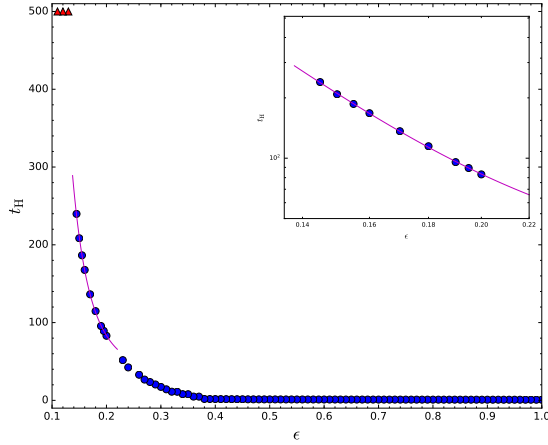
¹Except for poor fits as described in our discussion of the irregular phase.



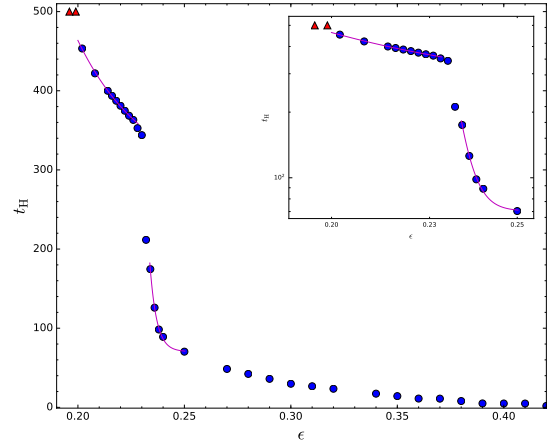
(a) $\mu = 15, \sigma = 1.5$



(b) $\mu = 5, \sigma = 1.7$



(c) $\mu = 0, \sigma = 1.8$



(d) $\mu = 0.5, \sigma = 1.7$

Figure 2.4: Metastable behavior: blue dots represent horizon formation and red triangles a lower limit on t_H . Magenta curves are fits $t_H = a\epsilon^{-p} + b$ over the shown range of amplitudes. See table 2.1 for best fit parameters.

The fits $t_H = a\epsilon^{-p} + b$ allow us to explore the time scale of horizon formation across the phase diagram, for example through a contour plot of one of the coefficients vs σ and μ . In most cases, this has not been informative, but an intriguing feature emerges if we plot the normalization coefficient a vs σ for unstable initial data at small σ , as shown in figure 2.3 for $t_{fit} = 60$. By eye, the coefficient is reasonably well described by the fit $a = 32.0(3)\sigma^{-2.01(2)}$ (values in parentheses are standard errors of the best fit values) *independent of scalar field mass*. This is not born out very well quantitatively; the reduced χ^2 for the fit is $\chi^2/\text{d.o.f.} = 180$, indicating a poor fit. However, the large χ^2 seems largely driven by a few outlier points with large scalar mass, so it is tempting to speculate that the gravitational collapse in this region of parameter space is driven by gradient energy, making all fields effectively massless at narrow enough initial σ . The picture is qualitatively similar if we consider the parameter a for $t_{fit} = 80, 100$ instead.

Several examples of metastable behavior appear in figure 2.4. These figures show both data

	a	p	b	$\chi^2/\text{d.o.f.}$
$\mu = 15, \sigma = 1.5$	0.10(1)	2.33(5)	-27(4)	0.7736
$\mu = 5, \sigma = 1.7$	0.89(5)	2.08(2)	-33(2)	0.3248
$\mu = 0, \sigma = 1.8$	0.06(2)	4.3(2)	30(5)	1.502
$\mu = 0.5, \sigma = 1.7$ ($t_H < 0.4t_{lim}$)	$4(32) \times 10^{-45}$	73(5)	70(2)	5.409
$(t_H > 0.72t_{lim})$	0.02(3)	5.6(8)	260(20)	1.078

Table 2.1: Best fit parameters for the cases shown in figure 2.4 restricting to $t_H > t_{fit} = 60$ and as noted. Values in parentheses are standard errors in the last digit. $\chi^2/\text{d.o.f.}$ is the reduced χ^2 value used as a measure of goodness-of-fit.

from the numerical evolutions (blue dots and red triangles) and fits of the form $t_H = a\epsilon^{-p} + b$ for points with $t_H > t_{fit} = 60$ (magenta curves). The best fit parameters are given in table 2.1.

Figures 2.4a, 2.4b demonstrate behavior typical of most of the instances of metastable initial data we have found; specifically, the initial data continue to collapse through horizon formation times of $t_H \sim 0.6t_{lim}$ but with p significantly greater than the perturbative value of $p = 2$. Note that the evolutions of figure 2.4b have been extended to larger values of t_H to demonstrate that the evolutions continue to collapse to somewhat smaller amplitude values. Figure 2.4b is also of interest because its best fit value $p \approx 2.08$ is approximately as close to the perturbative value as several stable sets of initial data but has a smaller standard error for the fit, so the difference from the perturbative value is more significant.

Figure 2.4c shows metastable evolution to $t_H \lesssim 0.6t_{lim}$ but then a sudden jump to stability until $t = t_{lim}$. In the figure, the fit has been extended to the largest non-collapsing amplitude, which demonstrates that there is no collapse over a time period significantly longer than the fit predicts. This example argues that metastable data may in fact become stable at the smallest amplitudes. On the other hand, figure 2.4d shows a similar jump in t_H to values $t_H < t_{lim}$; evolution at lower amplitudes shows metastable scaling with $p \approx 6$ for $360 < t_H < t_{lim}$. The figure also shows a metastable fit with larger reduced χ^2 at larger amplitudes corresponding to $t_{fit} < t_H < 0.4t_{lim}$. So this is another option: metastable behavior may transition abruptly to metastable behavior with different scaling (or possibly even perturbatively unstable behavior) at sufficiently small amplitudes. It is also reasonable to classify this case as irregular due to the sudden jump in t_H ; we choose metastable due to the clean metastable behavior at low amplitudes.

2.4.2 Behaviors of the irregular phase

We have found a variety of irregular behaviors at the transition between the metastable and stable phases which we have classified together as the irregular phase; however, it may be better to describe them as separate phases. The phase diagram 2.2 indicates that the irregular phase extends along the “inland” side of the small σ shoreline and at least part of the large σ shoreline of the island of stability. What is not clear from our evolutions up to now is whether each type of behavior appears along the entire shoreline or if they appear in pockets at different scalar field masses. Examples of each type of behavior that we have found appear in figure 2.5.

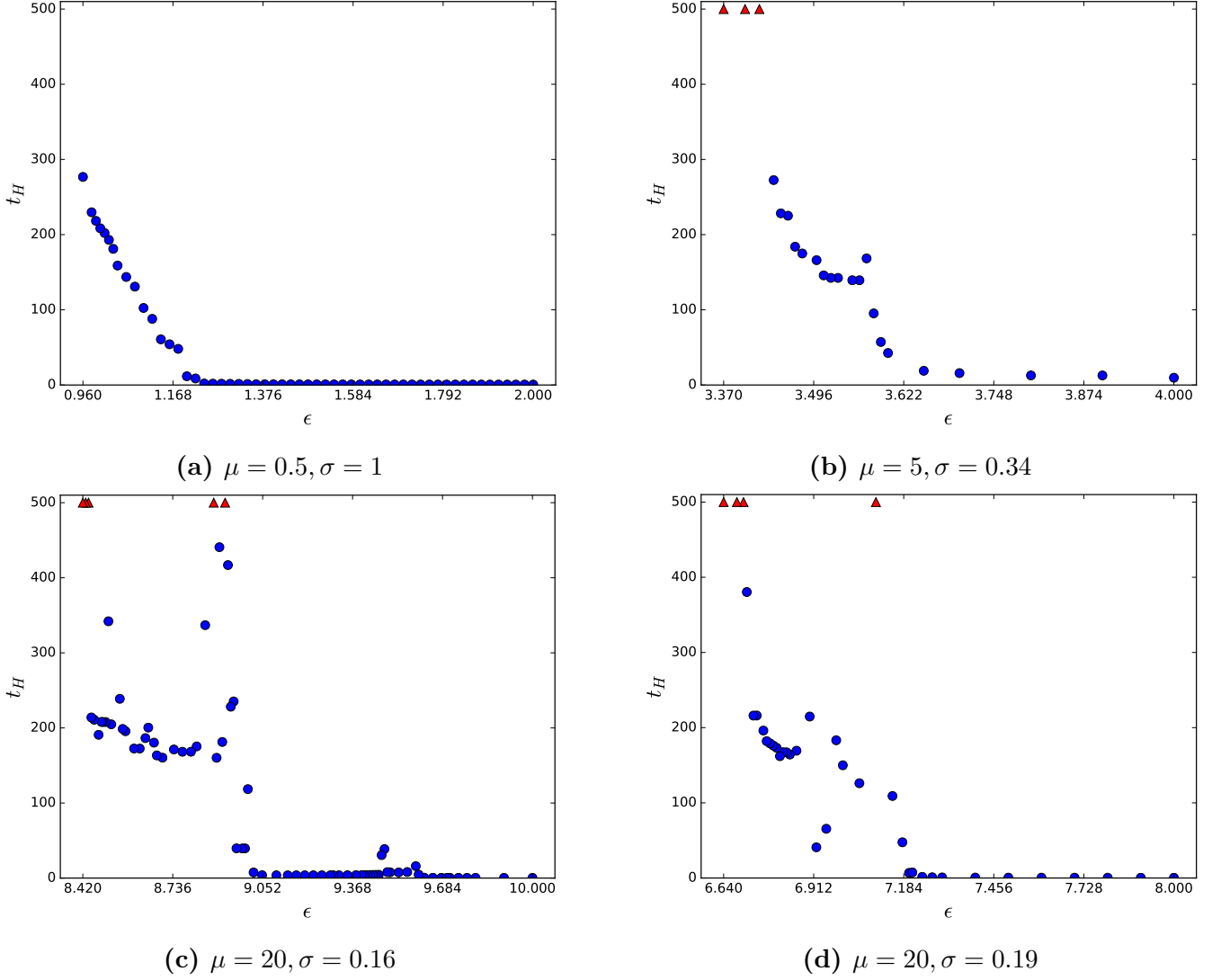
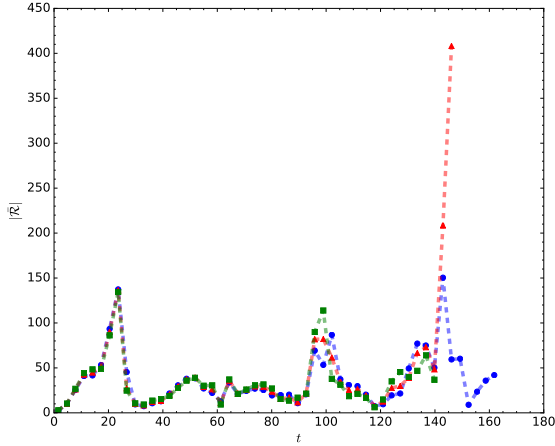


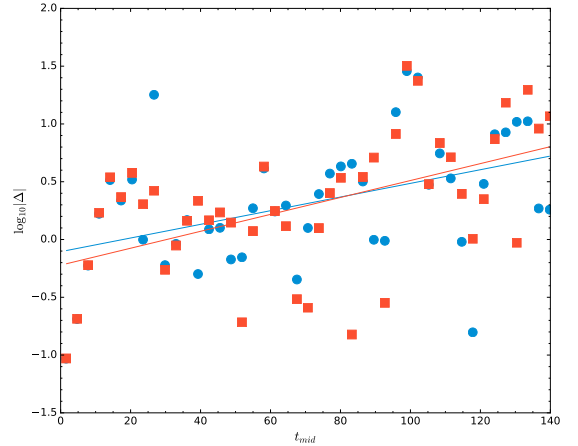
Figure 2.5: *Irregular behavior: blue dots represent horizon formation and red triangles a lower limit on t_H .*

The first type of irregular behavior, shown in figure 2.5a, is monotonic (t_H increases with decreasing ϵ as usual), but it is not well fit by a power law. In fact, this behavior would classify as metastable by the criterion of section 2.4.1 in that the power law of the best fit $t_H = a\epsilon^{-p} + b$ is significantly different from $p = 2$, except for the fact that the reduced χ^2 value for the fit is very large (greater than 10) and also that different fitting algorithms can return significantly different fits, even though the data may appear to the eye like a smooth power law. In any case, this type of behavior apparently indicates a breakdown of metastable behavior and hints at the appearance of non-monotonicity. So far, our evolutions have not demonstrated sudden jumps in t_H typical of stability at low amplitudes, however.

Figure 2.5b exemplifies non-monotonic behavior in the irregular phase. This type of behavior, which was noted already by [18], involves one or more sudden jumps in t_H as ϵ decreases, which may be followed by a sudden decrease in t_H and then resumed smooth monotonic increase in t_H . There are suggestions that this type of initial data is stable at low amplitudes due to the usual



(a) Upper envelope of Ricci scalar at origin



(b) $\log |\Delta|$ vs. t_{mid}

Figure 2.6: Left: The upper envelope of the Ricci scalar for amplitudes $\epsilon_1 = 3.50$ (blue circles), $\epsilon_2 = 3.51$ (red triangles), and $\epsilon_3 = 3.52$ (green squares) for $\mu = 5, \sigma = 0.34$. Right: $\log(|\Delta_{12}|)$ and best fit (blue circles and line) and $\log(|\Delta_{23}|)$ and best fit (red squares and line), calculated as a function of the midpoint t_{mid} of the time interval.

appearance of non-collapsing evolutions, but it is worth noting that these amplitudes could instead experience another jump and decrease in t_H , just at $t_H > t_{lim}$. Finally, [34] studied this type of behavior in some detail, denoting it as “quasi-stable.”

The last type of irregular behavior is apparently chaotic, in that t_H appears to be sensitive to initial conditions (ie, value of amplitude) over some range of amplitudes. This type of behavior appears over the range of masses (see figure 2.1d for a mild case for massless scalars), but it is more common and more dramatic at larger μ . Figures 2.5c, 2.5d represent the most extreme chaotic behavior among the initial data that we studied with collapse at $t_H < 50$ not very far separated from amplitudes that do not collapse for $t < t_{lim}$ along with an unpredictable pattern of variation in t_H . This type of chaotic behavior has been seen previously in the collapse of transparent but gravitationally interacting thin shells in AdS [39] as well as in the collapse of massless scalars in AdS₅ Einstein-Gauss-Bonnet gravity [30, 31]. In both cases, the chaotic behavior is hypothesized to be due to the transfer of energy between two infalling shells, with horizon formation only proceeding when one shell is sufficiently energetic. In the latter case, the extra scale of the theory (given by the coefficient of the Gauss-Bonnet term in the action) leads the single initial pulse of scalar matter to break into two pulses.

We should therefore ask two questions: does this irregular behavior show evidence of true chaos, and is a similar mechanism at work here? To quantify the presence of chaos, we examine the difference in time evolution between similar initial conditions (nearby amplitudes), which diverge exponentially in chaotic systems. Specifically, any quantity Δ should satisfy $|\Delta| \propto \exp(\lambda t)$ for Lyapunov coefficient λ . Our characteristic will be the upper envelope of the Ricci scalar at the origin per light crossing time, $\bar{\mathcal{R}}(t)$. We consider the chaotic behavior exhibited by three states: a massless scalar of width $\sigma = 1.1$ with amplitudes $\epsilon = 1.02, 1.01, 1.00$ (see figure 2.1d), a $\mu = 5$ massive scalar of width $\sigma = 0.34$ and $\epsilon = 3.52, 3.51, 3.50$, and a $\mu = 20$ scalar of width $\sigma = 0.19$ and $\epsilon = 6.98, 6.95, 6.92$ (figure 2.5d).

		λ	average λ
$\mu = 0, \sigma = 1.1$	Δ_{12}	0.011(6)	0.011
	Δ_{23}	0.011(5)	
$\mu = 5, \sigma = 0.34$	Δ_{12}	0.006(2)	0.007
	Δ_{23}	0.007(2)	
$\mu = 20, \sigma = 0.19$	Δ_{12}	0.046(9)	0.032
	Δ_{23}	0.019(7)	

Table 2.2: Best fit Lyapunov coefficients λ for adjacent amplitude pairs and average λ value for each μ, σ system studied. The parenthetical value is the error in the last digit.

Figure 2.6 details evidence for chaotic evolution in the $\mu = 5, \sigma = 0.34$ case; figure 2.6a shows our characteristic function $\bar{\mathcal{R}}(t)$ for the amplitudes $\epsilon_1 = 3.50$, $\epsilon_2 = 3.51$, and $\epsilon_3 = 3.52$. By eye, $\bar{\mathcal{R}}$ shows noticeable differences after a long period of evolution. These are more apparent in figure 2.6b, which shows the log of the differences $\Delta_{ab} \equiv \bar{\mathcal{R}}_{\epsilon_a} - \bar{\mathcal{R}}_{\epsilon_b}$, along with the best fits. Although there is considerable noise — or oscillation around exponential growth — in the differences (leading to R^2 values $\sim 0.2, 0.26$ for the fits), the average slope gives Lyapunov coefficient $\lambda = 0.007$ (within the error bar of each slope), and each slope differs from zero by more than 3 standard errors. One interesting point is that the t_H vs ϵ curve in figure 2.5b does not appear chaotic to the eye, even though it shows some of the mathematical signatures of chaos at least for $\epsilon_1 < \epsilon < \epsilon_3$, the amplitude values near the visible spike in t_H .

The story is similar for the massless and $\mu = 20$ cases we studied, which exhibit λ values that differ from zero by at least 1.9 standard deviations; see table 2.2. This is a milder version of the chaotic behavior noted by [30, 31, 39], especially for the $\mu = 5$ case studied. To our knowledge, this is the first evidence of chaos in the gravitational collapse of a massless scalar in AdS. One thing to note is that the strength of oscillation in $\log(|\Delta|)$ around the linear fit increases with increasing mass, so that the two best fit Lyapunov exponents for $\mu = 20$ are no longer consistent with each other at the 1-standard deviation level.

The mechanism underlying the chaotic behavior seems somewhat different or at least weaker than the two-shell or Einstein-Gauss-Bonnet systems. When examining the time evolution of the mass distributions of these data, we see a single large pulse of mass energy that oscillates between the origin and boundary without developing a pronounced peak. However, there is also apparently a smaller wave that travels across the large peak. In the massless case examined, this wave deforms the pulse, leading at times to the double-shoulder appearance of figure 2.7a. In the $\mu = 5, \sigma = 0.34$ case, the secondary wave is more like a ripple, usually smaller in amplitude but more sharply localized, as toward the right side of the main pulse in figure 2.7b. So the chaotic behavior may be caused by the relative motion of the two waves, rather than energy transfer between two shells. In this hypothesis, a horizon would form when both waves reach the neighborhood of the origin at the same time.

As a note, we have run convergence tests on several sets of irregular initial data and find that our calculations are convergent overall, as expected (even at lower resolution than we used). In

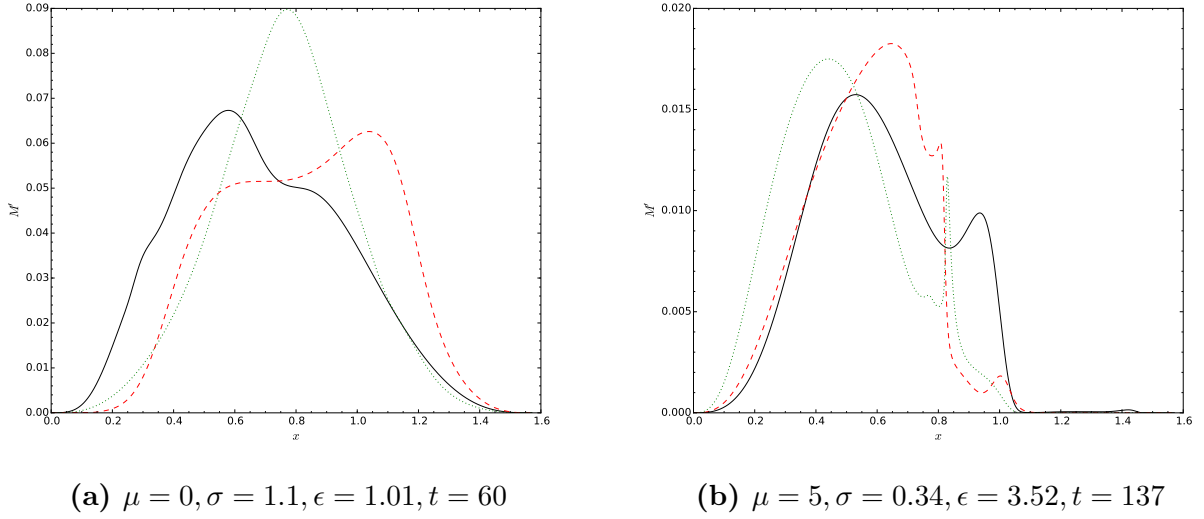


Figure 2.7: Radial derivative of the mass function at the indicated time for two chaotic systems. Note the appearance of a secondary wave on top of the main pulse. (μ, σ, ϵ) as indicated.

particular, the massless scalar evolutions studied in table 2.2 are convergent already at resolution given by $n = 12$ (note that we typically start at $n = 14$). The only caveat may be for some of the strongly chaotic initial data with scalar mass $\mu = 20$, which nonetheless appear well-behaved according to other indicators. The reader may or may not wish to take them at face value but should recall that we have presented other chaotic initial data with rigorously convergent evolutions. See the appendix for a more detailed discussion.

2.5 Spectral analysis

As we discussed in the introduction, instability toward horizon formation proceeds through a turbulent cascade of energy to shorter wavelengths or, more quantitatively, to 1st-order scalar eigenmodes with more nodes. Inverse cascades are typical of stable evolutions. Therefore, understanding the energy spectrum of our evolutions, both initially and over time, sheds light on the behavior of the self-gravitating scalar field in asymptotically AdS spacetime, providing a heuristic analytic understanding of the phase diagram.

The (normalizable) eigenmodes e_j are given by Jacobi polynomials as

$$e_j(x) = \kappa_j \cos^{\lambda_+}(x) P_j^{(d/2-1, \sqrt{d^2+4\mu^2}/2)}(\cos(2x)) \quad (2.8)$$

(κ_j is a normalization constant) with eigenfrequency $\omega_j = 2j + \lambda_+$ and $\lambda_+ = (d + \sqrt{d^2 + 4\mu^2})/2$ in AdS_{d+1} for $j = 0, 1, \dots$ (see [40, 41] for reviews). Including gravitational backreaction, we define the energy spectrum

$$E_j \equiv \frac{1}{2} \left(\Pi_j^2 - \phi_j \ddot{\phi}_j \right), \quad (2.9)$$

where

$$\begin{aligned} \Pi_j &= \left(\sqrt{A} \Pi, e_j \right), \quad \phi_j = (\phi, e_j), \\ \ddot{\phi}_j &= \left(\cot^{d-1}(x) \partial_x [\tan^{d-1}(x) A \Phi] - \mu^2 \sec^2(x) \phi, e_j \right), \end{aligned} \quad (2.10)$$

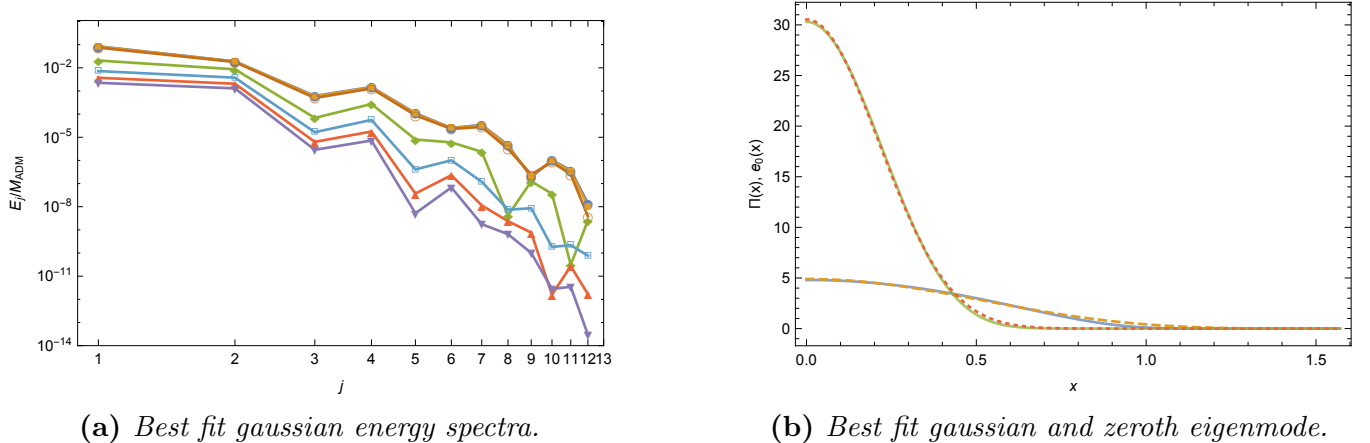


Figure 2.8: Left: Spectra of the best fit gaussians (2.7) to the $j = 0$ eigenmode for masses $\mu = 0$ (blue circles), 0.5 (yellow squares), 1 (empty orange circles), 5 (green diamonds), 10 (empty cyan squares), 15 (upward red triangles), and 20 (downward purple triangles). Right: an overlay of the best fit Gaussian and e_0 eigenmode for $\mu = 0$ (solid blue is best fit, orange dashed is eigenmode) and $\mu = 20$ (solid green, red short dashes).

and the inner product is $(f, g) = \int_0^{\pi/2} dx \tan^{d-1}(x) fg$. The sum of E_j over all modes is the conserved ADM mass.

2.5.1 Dependence on mass

The most visibly apparent feature of the phase diagram of figure 2.2 is that the island of stability both expands and shifts to smaller widths as the scalar mass increases. As it turns out, the energy spectrum of the Gaussian initial data (2.7) provides a simple heuristic explanation.

It is well established both in perturbation theory and numerical studies that initial data given by a single scalar linear-order eigenmode is in fact nonlinearly stable, and the spectra of many quasi-periodic solutions are also dominated by a single eigenmode. As a result, we should expect Gaussian initial data that approximates a single eigenmode (which must be $j = 0$ due to lack of nodes) to be stable. To explore how this depends on mass, we find the best fit values of ϵ, σ for the $j = 0$ eigenmode for each mass that we consider (defined by the least-square error from the Gaussian to a discretized eigenmode); this is the “best approximation” Gaussian to the eigenmode. Then we find the energy spectrum of that best-fit Gaussian; these are shown in figure 2.8a. From the figure, it is clear that the $j = 0$ eigenmode is closer to a Gaussian at larger masses. That is, other eigenmodes contribute less to the Gaussian’s spectrum at higher masses (by several orders of magnitude over the range from $\mu = 0$ to 20). Simply put, the shape of the $j = 0$ eigenmode is closer to Gaussian at higher masses, which suggests that the island of stability should be larger at larger scalar field mass. Figure 2.8b compares the $j = 0$ eigenmode and best fit Gaussian for $\mu = 0$ and 20; on inspection, there is more deviation between the eigenmode and Gaussian for the massless scalar.

In addition, the best-fit Gaussian width decreases from $\sigma \sim 0.8$ for a massless scalar as the mass increases. At $\mu = 20$, the best-fit width is $\sigma \sim 0.31$. This suggests that Gaussians that approximate the $j = 0$ mode well enough are narrower in width at higher masses. An interesting point to note is that the island of stability for $\mu = 0, 0.5$ is actually centered at considerably larger

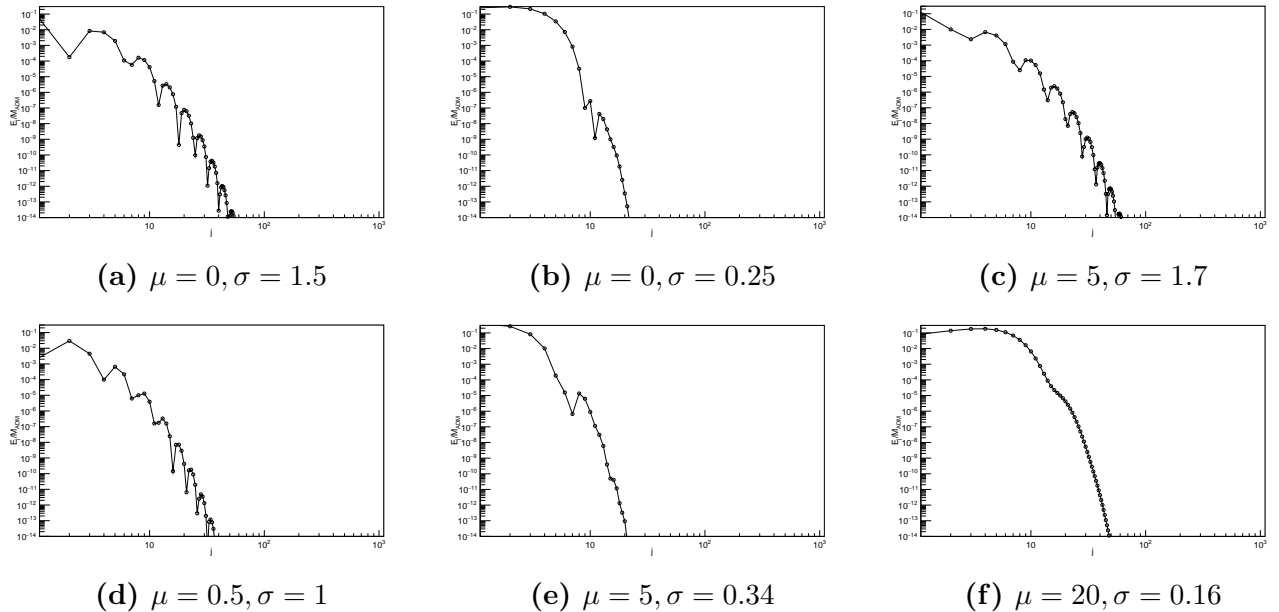


Figure 2.9: Initial ($t = 0$) energy spectra for the indicated evolutions. In order, these represent stable, unstable, metastable, monotonic irregular, non-monotonic irregular, and chaotic irregular initial data.

widths than the best-fit Gaussian. This may not be surprising, since the best-fit Gaussians at low masses actually receive non-negligible contributions from higher mode numbers; moving away from the best-fit Gaussian can actually reduce the power in higher modes. For example, the stable initial data shown in figure 2.9a below has considerably less power in the $j = 2$ mode.

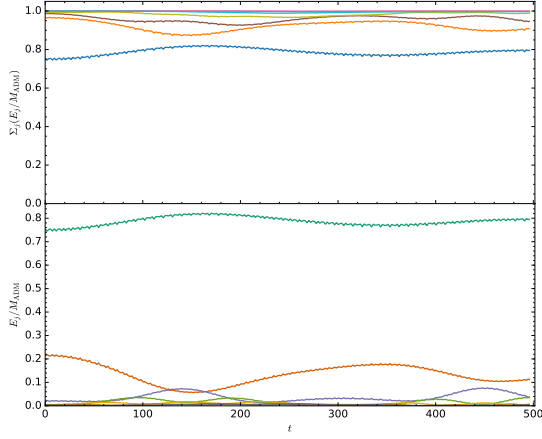
2.5.2 Spectra of different phases

A key question that one might hope to answer is whether the stability phase of a given (μ, σ) can be determined easily by direct inspection of the initial data without requiring many evolutions at varying amplitudes. The initial energy spectra for examples of each phase, including monotonic, non-monotonic, and chaotic irregular behaviors, are shown in figure 2.9. These spectra are taken from among the smallest amplitudes we evolved in order to minimize backreaction effects.

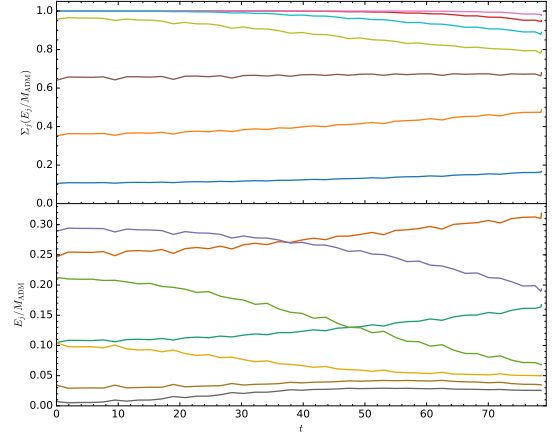
Unfortunately, the initial energy spectra do not seem to provide such a method for determining the stability phase. Very broadly speaking, stable and metastable (μ, σ) correspond to initial spectra that drop off fairly quickly from the $j = 0$ mode as j increases, while unstable and irregular phases tend to have roughly constant or even slightly increasing spectra up to $j = 5$ or 10. However, figure 2.9d shows that some irregular initial data have spectra that decrease rapidly after a small increase from $j = 1$ to $j = 2$. Kinks in the spectrum are more prevalent for widths of the AdS scale or larger, while spectra for smaller widths tend to be smoother.

2.5.3 Evolution of spectra

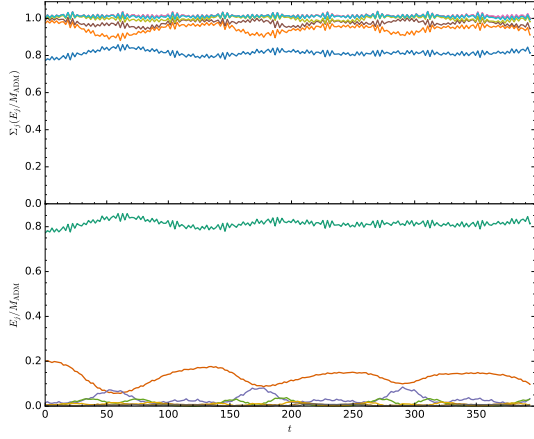
While the initial spectrum for a given (μ, σ) pair does not have predictive value regarding the future behavior as far as we can tell, the time dependence of the spectrum throughout the evolution of the system is informative. Figure 2.10 shows the time-dependence of spectra for examples of the



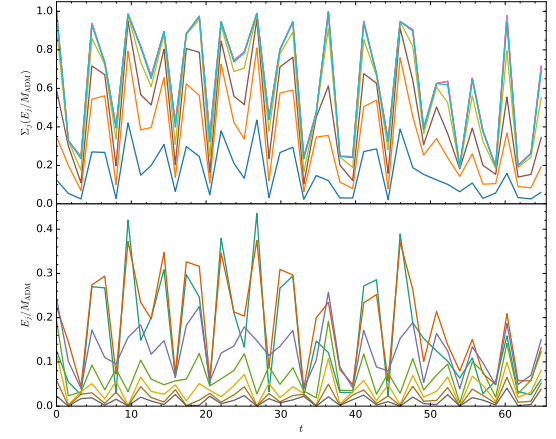
(a) $\mu = 0, \sigma = 1.8, \epsilon = 0.13$



(b) $\mu = 0, \sigma = 0.25, \epsilon = 2.28$



(c) $\mu = 0.5, \sigma = 1.7, \epsilon = 0.216$



(d) $\mu = 20, \sigma = 0.19, \epsilon = 6.95$

Figure 2.10: The time dependence of the energy spectra as a fraction of the total ADM mass for the indicated μ, σ, ϵ . Lower panels show the lowest 7 modes (in colors cyan, red, purple, green, yellow, brown, and gray respectively). Upper panels show cumulative energy to mode $j = 0, 1, 2, 4, 8, 16, 32$ (in colors blue, orange, brown, yellow, aqua, red, and magenta).

stable, unstable, metastable, and chaotic irregular phases. In each figure, the lower panel shows the fraction E_j/M_{ADM} in each mode up to $j = 6$, while the upper panel shows the cumulative fraction $\sum_j E_j/M_{ADM}$ to the mode 2^k with $k = 0$ to 5.

The difference between stable evolution in figure 2.10a and unstable evolution in figure 2.10b is readily apparent. As the evolution proceeds, we expect a cascade of energy into higher mode numbers, but inverse cascades to lower modes can also occur. The stable evolution shows a slow pattern of cascades and inverse cascades, in fact. On the other hand, the unstable evolution shows a nearly monotonic cascade of energy into the highest modes along with a simultaneous cascade of energy into the lowest modes (therefore depleting intermediate modes). These are common observations in the literature and are included here for completeness.

The metastable evolution shown in figure 2.10c is interesting in light of the stable and unstable

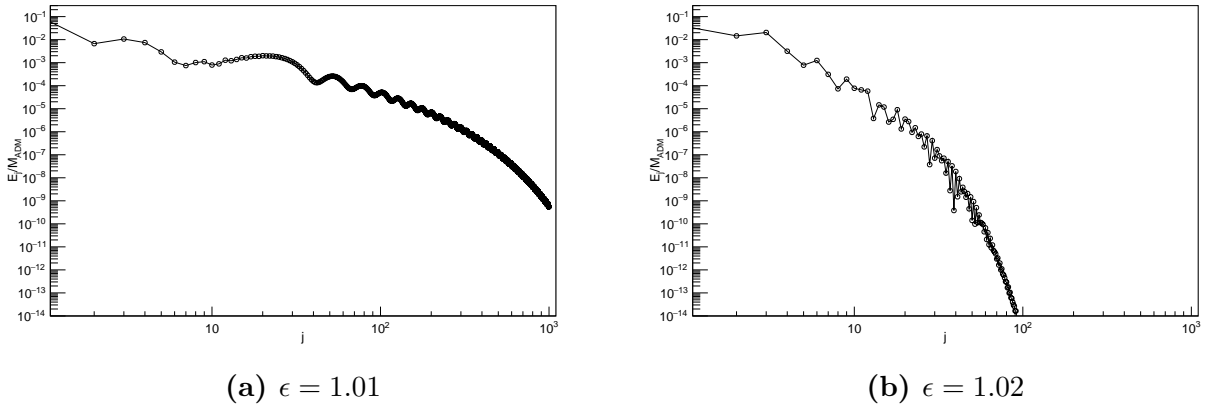


Figure 2.11: Spectra at time $t \approx 71$ for $\mu = 0, \sigma = 1.1$ for the two amplitudes given. $\epsilon = 1.01$ forms a horizon at $t_H \approx 71.1$, $\epsilon = 1.02$ at $t_H \approx 248.0$.

spectra. The amplitude shown is from the “unstable” portion of figure 2.4d, the part consistent with the perturbative scaling $t_H \sim \epsilon^{-2}$. However, the spectrum shows a similar pattern of slow cascades and inverse cascades to the stable phase example, though on a somewhat faster time scale in this case. While perhaps surprising, this is in keeping with the similarities noted between the initial spectra in figures 2.9a and 2.9c. We have also checked that the time-dependent spectrum at a higher amplitude with $t_H \sim 100$ follows the same pattern as 2.10c; in fact, it looks essentially the same but simply ends at an earlier time. This lends some credence to the idea that the metastable phase is stable at lowest nontrivial order in perturbation theory, with instability triggered by higher-order corrections. Alternately, the instability could be caused by an oscillatory singularity in the perturbative theory, as discussed in [15, 23–25] in the case of two-mode initial data. These divergences do not appear in the energy spectrum.

Figure 2.10d shows the time-dependence of the spectrum in a chaotic irregular evolution, specifically $\mu = 20, \sigma = 0.19$ at $\epsilon = 6.95$, which is in the chaotic region of the t_H vs ϵ plot in figure 2.5d. There is rapid energy transfer among modes, including cascades out of and inverse cascades into mode numbers $j \leq 32$ over approximately a light-crossing time. It is easy to imagine that horizon formation might occur at any of the cascades of energy into higher modes, leading to seemingly random jumps in t_H as a function of amplitude.

Finally, the time-evolved energy provide another possible measure of approximate thermalization in the dual CFT; namely, the spectrum should approach an (exponentially cut-off) power law at thermalization. In most cases, this occurs shortly before horizon formation, but there are exceptions, such as the late time behavior of initial data below the critical mass for black hole formation in Einstein-Gauss-Bonnet gravity [30]. In the case of chaotic behavior, it is particularly interesting to know if the spectra for similar amplitudes approach a power law at similar times even if horizons form at very different times. Figure 2.11 shows the energy spectra for two amplitudes in the chaotic region of the t_H vs ϵ plot for $\mu = 0, \sigma = 1.1$. Figure 2.11a is the spectrum just before horizon formation for $\epsilon = 1.01$, while figure 2.11b is the spectrum at approximately the same time for $\epsilon = 1.02$, which is very long before horizon formation. In this example, we see that the spectrum does approach a power law for the evolution that is forming a horizon, while the other evolution demonstrates apparently exponential decay. Therefore, this example suggests that a power law spectrum may yield similar results to horizon formation as a measure of thermalization in the dual

CFT.

2.6 Discussion

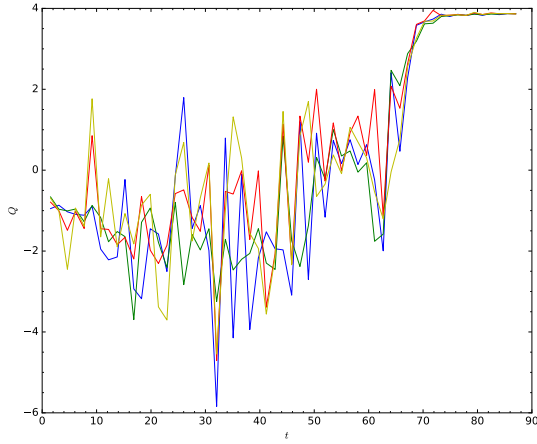
We have presented the phase diagram of stability of AdS_5 against horizon formation, treating the scalar field mass μ and width σ of initial data as free parameters. In addition to mapping the location of the so-called “island of stability,” we have gathered evidence for two non-perturbative phases on the “shorelines” of the island, the metastable and irregular phases. While these must either exhibit stability (no collapse below some critical amplitude) or instability (collapse at arbitrarily small but finite amplitude) as the amplitude $\epsilon \rightarrow 0$, they are distinguished by their behavior at computationally accessible amplitudes. While perturbatively unstable evolutions obey $t_H \propto \epsilon^{-2}$ as $\epsilon \rightarrow 0$, metastable initial data follows $t_H \propto \epsilon^{-p}$ for $p > 2$ over a range of amplitudes. The irregular phase is characterized by horizon formation times t_H that are not well described by a power law and sometimes exhibit non-monotonicity or even chaos. Both of these phases appear across the range of μ values that we study and at both small- and large-width boundaries of the stable phase.

At this time, it is impossible to say whether metastable initial data is stable or unstable as $\epsilon \rightarrow 0$ (or if all metastable data behaves in the same way in that limit). Our numerical evolutions include cases in which the lowest amplitudes jump either to metastable scaling with smaller p or to evolutions that do not collapse over the timescales we study. In many cases, too, the power law $t_H \propto \epsilon^{-p}$ with p some fixed value > 2 is robust as we exclude larger amplitudes from our fit. It is also possible that some of the metastable phase is stable in the perturbative theory (ie, to ϵ^3 order in a perturbative expansion) but not at higher orders.

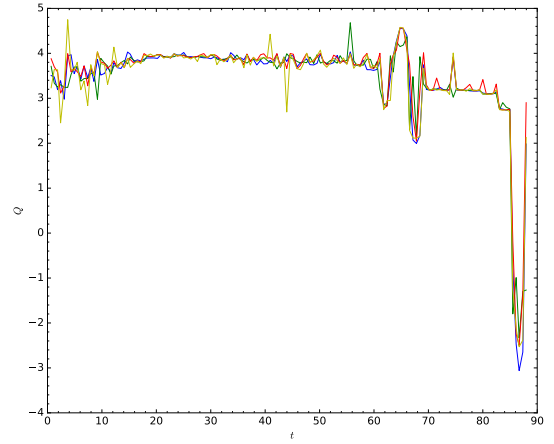
The irregular phase seems likely to be (mostly) stable at arbitrarily small amplitudes based on our numerical evolutions, though we have not found a critical amplitude for monotonic irregular initial data. The irregular phase includes the “quasi-stable” initial data described in [18, 34], which has a sudden increase then decrease in t_H as ϵ decreases as well as truly chaotic behavior. In fact, we have found evidence for weakly chaotic behavior at the jump in t_H for non-monotonic initial data in the form of a small but nonzero Lyapunov coefficient. Both non-monotonicity and chaos become stronger and more common at larger scalar masses; however, we have also found chaotic behavior for the massless scalar. To our knowledge, this is the first evidence of chaos in spherically symmetric massless scalar collapse in AdS, which is particularly interesting because there is only one physically meaningful ratio of scales, σ as measured in AdS units.

Aside from the ultimate stability or instability of the metastable and irregular phases, several questions remain. For one, black holes formed in massive scalar collapse in asymptotically flat space-time exhibit a mass gap for initial profiles wider than the Compton wavelength $1/\mu$ [42]. Whether this mass gap exists in AdS is not clear, and it may disappear through repeated gravitational focusing as the field oscillates many times across AdS; investigating this type of critical behavior will likely require techniques similar to those of [43]. Returning to our phase diagram, the physical mechanism responsible for chaos in the irregular phase is not yet clear. Is it some generalization of the same mechanism as found in the two-shell system? Also, would an alternate definition of approximate thermalization in the dual CFT, such as development of a power-law spectrum, lead to a different picture of the phase diagram? Finally, the big question is whether there is some test that could be performed on initial data alone that would predict in advance its phase? So far, no test is entirely successful, so new ideas are necessary.

Acknowledgments We would like to thank Brayden Yarish for help submitting jobs for the $\mu = 10$ evolutions. The work of ND is supported in part by a Natural Sciences and Engineering Research Council of Canada PGS-D grant to ND, NSF Grant PHY-1606654 at Cornell University, and by a grant from the Sherman Fairchild Foundation. The work of BC and AF is supported by the Natural Sciences and Engineering Research Council of Canada Discovery Grant program. This research was enabled in part by support provided by WestGrid (www.westgrid.ca) and Compute Canada Calcul Canada (www.computecanada.ca).



(a) $n = 14$ base resolution



(b) $n = 11$ base resolution

Figure 2.A.1: Convergence results for $\mu = 0.5$, $\sigma = 1$, $\epsilon = 1.12$ showing order of convergence Q vs time for ϕ, M, A, δ (blue, green, red, yellow respectively). Left: Resolutions $n = 14, 15, 16$ used. Right: Resolutions $n = 11, 12, 13$ used.

Appendix

2.A Convergence Testing

Due to the large number of evolutions we have carried out, it is not computationally feasible to test all of them for convergence. Therefore, we have checked several interesting cases from the irregular phase, which are the most curious. These are carried out by evolving the initial data with a base resolution $n = 14$ and again at $n = 15, 16$ with commensurate time steps, as described in [34]. In the cases indicated, we evaluated the order of convergence at lower resolutions. We remind the reader that the order of convergence Q is the base-2 logarithm of the ratio of L^2 errors (root-mean-square over all corresponding grid points) between successive pairs of resolutions. We also note that the initial data is defined analytically, so Q can appear poor at $t = 0$ since the errors are controlled by round off; in some cases, Q is therefore undefined and not plotted.

First, we carried out convergence tests for mass $\mu = 0.5$, width $\sigma = 1$, and amplitude $\epsilon = 1.12$, which is monotonic irregular initial data presented in figure 2.5a. This amplitude collapses with $t_H \sim 88$. Figure 2.A.1a shows the (L^2 norm) order of convergence for the field variable ϕ , the mass function M , and the metric functions A, δ . While the order of convergence is initially poor and even negative, all these variables show approximately fourth order convergence for times $t \gtrsim 70$. The reason for the initially poor convergence is that the error between successive resolutions is already

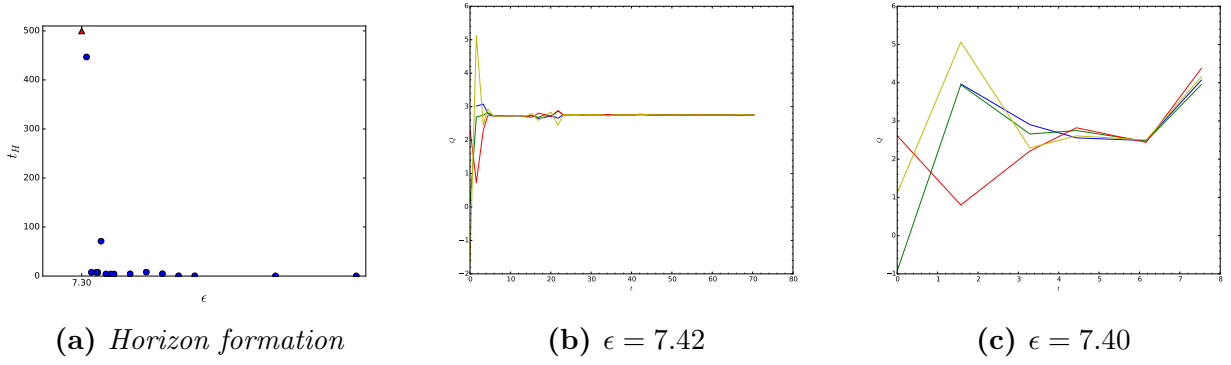


Figure 2.A.2: Convergence results for $\mu = 15$, $\sigma = 0.2$. Left: t_H vs ϵ . Middle & Right: order of convergence vs time for ϕ, M, A, δ (blue, green, red, yellow respectively) for indicated amplitudes.

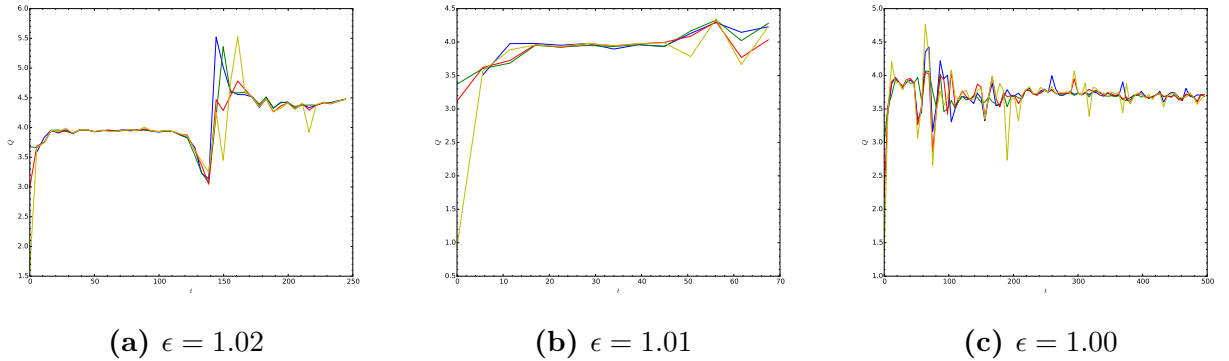


Figure 2.A.3: Convergence results for $\mu = 0$, $\sigma = 1.1$ for listed amplitudes showing order of convergence Q vs time for ϕ, M, A, δ (blue, green, red, yellow respectively); resolutions $n = 12, 13, 14$.

given by (machine limited) round off. As a demonstration, we tested the order of convergence with base resolution $n = 11$, as shown in figure 2.A.1b. The variables show order of convergence $Q \gtrsim 3$ already at this resolution for most of the evolution, losing convergence only for $t > 80$, where we see approximately 4th-order convergence in the $n = 14$ resolution computations.

Two of the authors have discussed the convergence properties of evolution for the nonmonotonic irregular initial data with $\mu = 20, \sigma = 0.1, \epsilon = 11.74$, which is in an amplitude region of increased t_H surrounded by smaller values, in detail in [34]. In short, the variables ϕ, M, A, δ all exhibit fourth order convergence, as does $\Pi^2(t, 0)$, and the conserved mass actually has 6th order convergence.

Initial data for $\mu = 15, \sigma = 0.2$ is also nonmonotonic, as shown in figure 2.A.2a. While we have not analyzed all aspects of the convergence, we see from the remainder of figure 2.A.2 that ϕ, M, A, δ exhibit convergent behavior at better than second order for $\epsilon = 7.42$ (figure 2.A.2b, second-largest value of t_H in figure 2.A.2a) and $\epsilon = 7.40$ (figure 2.A.2c, adjacent amplitude in figure 2.A.2a). It is important to note that the larger amplitude also has the larger horizon formation time, contrary to the usual monotonic behavior.

It is most crucial to validate the convergence of chaotic evolutions. In table 2.2, we noted that the Ricci scalar at the origin has nonzero Lyapunov exponent at almost the 2 sigma level for amplitudes $\epsilon = 1.02, 1.01, 1.00$ for $\mu = 0, \sigma = 1.1$. We show the results of convergence tests for these amplitudes in figure 2.A.3; because these are longer evolutions, we consider the convergence

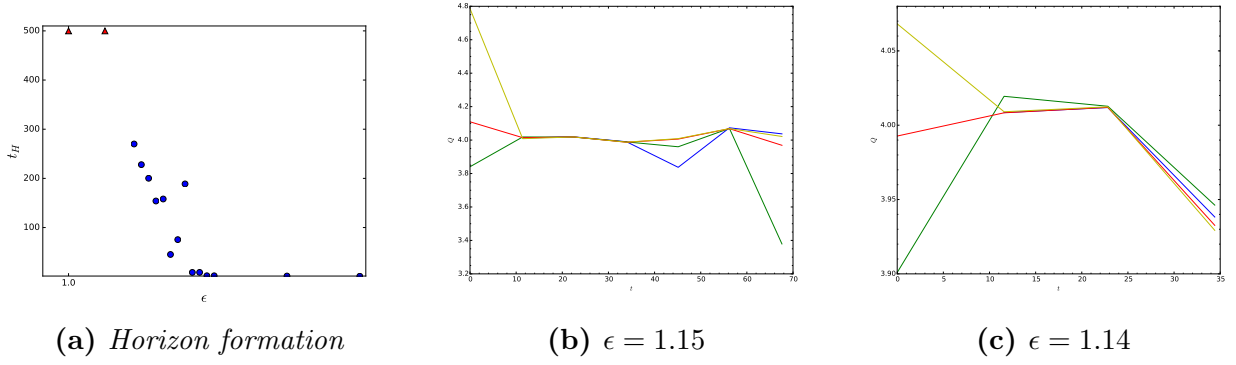


Figure 2.A.4: Convergence results for $\mu = 1, \sigma = 1$. Left: t_H vs ϵ . Middle & Right: order of convergence Q vs time for ϕ, M, A, δ (blue, green, red, yellow respectively); resolutions $n = 11, 12, 13$.

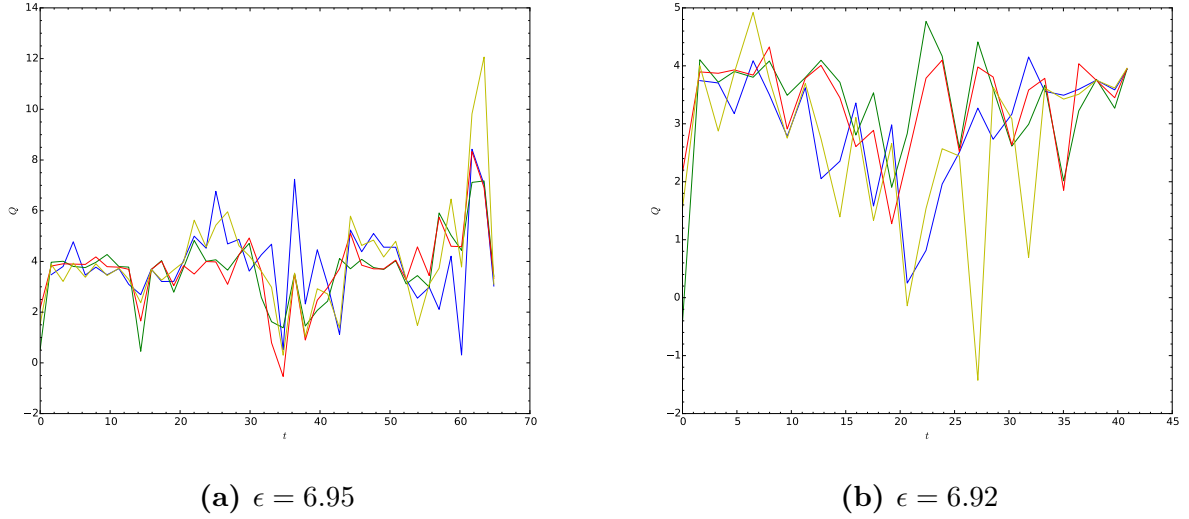


Figure 2.A.5: Order of convergence vs time for ϕ, M, A, δ (red, blue, green, magenta) for $\mu = 20, \sigma = 0.19$ and indicated amplitudes.

at the lower resolutions $n = 12, 13, 14$. After a transient start-up period, these are all convergent with $Q > 2.5$ for all variables considered at all times; for most of the time, the order of convergence is $Q > 3.5$. It is worth noting that one of the amplitudes does not form a horizon through $t = 500$.

Initial data with $\mu = 1, \sigma = 1$ is chaotic over a narrow range of amplitudes. We have carried out convergence testing for amplitudes $\epsilon = 1.15, 1.14$, which are the two amplitudes with $t_H < 100$ between amplitudes with $t_H \gtrsim 150$ in figure 2.A.4a. The order of convergence was poor for these amplitudes in our initial tests with base resolution $n = 14$ because the error between resolutions was dominated by round-off, similar to the convergence tests we discussed above for $\mu = 0.5, \sigma = 1$. In subsequent tests with lower resolutions $n = 11, 12, 13$, we find an order of convergence $Q \sim 4$ for most of the evolutions (and always $Q > 3$). It is important to note again that our evolutions exhibit convergence while showing horizon formation at a later time for a larger amplitude in this case.

Finally, we ran convergence tests for the chaotic initial data with $\mu = 20, \sigma = 0.19$ for $\epsilon = 6.95, 6.92$, with $t_H \approx 65.5, 40.8$ respectively. As shown in figure 2.A.5, the simulations are close

to fourth order convergence for most of the evolution, but there are periods where the order of convergence for evolution and constraint variables becomes negative. This of course leads to the concern that the evolutions should have collapsed during those periods and extend into an “afterlife” evolution. We have therefore evolved these amplitudes through these regions (approximately $t = 30 - 40$ for $\epsilon = 6.95$ and $t = 18 - 30$ for $\epsilon = 6.92$) at high resolution ($n = 18$). If the evolutions are truly in an afterlife, this higher resolution calculation may include horizon formation. We do not observe this. Another tell-tale of would-be horizon formation is a decrease in the timestep size by an order of magnitude or more followed by an increase. We monitor the timestep size every 500 timesteps through this evolution but do not observe a decrease in timestep size by more than a factor of 2. As a result, we believe the values of t_H found are reliable, though the reader may wish to consider them with some caution. Nonetheless, we emphasize that we have found convergent behavior for chaotic initial data at other scalar masses.

3 Perturbative Stability of Massless Scalars in AdS_4

Will be published to the arXiv, then submitted to JHEP

3.1 Contributions

What my contributions were

Paper Title

To Appear on arxiv.org

Brad Cownden¹, Nils Deppe², and Andrew R. Frey^{3,4}

¹*Department of Physics & Astronomy,
University of Manitoba
Winnipeg, Manitoba R3T 2N2, Canada
cowndenb@myumanitoba.ca*

²*Cornell Center for Astrophysics and Planetary Science and Department of Physics,
Cornell University
122 Sciences Drive, Ithaca, New York 14853, USA
nd357@cornell.edu*

³*Department of Physics & Astronomy,
University of Manitoba
Winnipeg, Manitoba R3T 2N2, Canada*

⁴*Department of Physics and Winnipeg Institute for Theoretical Physics,
University of Winnipeg
515 Portage Avenue, Winnipeg, Manitoba R3B 2E9, Canada
a.frey@uwinnipeg.ca*

We construct a family of perturbative solutions for massless scalar fields in AdS_4 using the *Two-Time Formalism* (TTF) to high eigenmode numbers. We furthermore investigate the validity of *quasi-periodic* (QP) solutions with high j_{\max} values and examine their stability to perturbations. Finally, check that TTF and QP solutions continue to satisfy the Einstein equation at times greater than $t \sim \epsilon^{-2}$ and compare these results to the full numerical solutions at low amplitude.

3.2 Introduction

The question of the nonperturbative stability of AdS_{d+1} has been examined extensively, both as a question of mathematical physics and given its application to the AdS/CFT correspondence; see [44] for a recent review. Beginning with the seminal work of [1], many works [2–4, 45, 46] have demonstrated the generic instability of AdS_{d+1} gravity minimally coupled to a scalar field in a variety of dimensions. The primary driver of the instability in the fully nonlinear system is the weakly turbulent flow of energy to short length scales; in the perturbative description, secular growth of resonant terms with high frequencies triggers the collapse [5, 28, 47]. However, [19, 48, 49] (and others) have shown that some initial conditions in asymptotically AdS spacetime resist gravitational collapse and therefore form islands of stability in the space of initial data. The stable solutions within the island are variously known as oscillons or breathers for real scalars [1, 45, 48, 50], boson stars for complex scalars [18, 19], and geons for pure gravity [5, 51].¹ [34, 52, 53] have shown that the classification of initial data is more complex nonperturbatively, intriguingly finding evidence of

¹citations given for studies in asymptotically AdS space.

chaos at the boundary between stable and unstable initial data. While past studies have mostly dealt with spherically symmetric collapse, an increasing amount of work is focused on removing this restriction [54–56].

While the nonperturbative physics of AdS instability requires numerical study, a perturbative formulation should give insight into stability at low amplitudes. In a naive perturbation theory, the fully resonant spectrum of eigenmodes of pure AdS leads to secular growth; this can be removed order by order by frequency shifts if the initial data consists of a single eigenmode but not for superpositions of eigenmodes [5]. If instead the amplitude and phase of each eigenmode are allowed to flow slowly, resummation of the perturbation theory leads to a ladder of coupled first-order ordinary differential equations describing the flow. There are several equivalent methods to arrive at the flow equations: a “two-time formalism” (similar to a temporal gradient expansion for the amplitude and phase variables) [6], a renormalization-like formalism [7, 11], time averaging [11, 17], and keeping only resonant source terms [23]. (We will commonly refer to the perturbative theory as the TTF theory, for two-time formalism.) A key feature of this perturbative theory is a scaling symmetry $\phi(t) \rightarrow \epsilon^{-1}\phi(\epsilon^2 t)$, so it is possible to divide out the amplitude of the scalar and describe the solution in terms of the “slow time” $\tau = \epsilon^2 t$. Furthermore, the perturbative theory has conserved quantities beyond the total energy E , including a “particle number” N , which leads to inverse cascades in energy from higher eigenmodes to lower modes along with the expected direct cascades from low to high. On the other hand, while the flow equations are significantly less computationally intensive than the full Einstein and Klein-Gordon equations, finding a solution requires truncating to a maximum eigenmode number j_{max} .

At a given mode truncation j_{max} , the TTF theory has stable quasi-periodic (QP) solutions with constant energy spectrum as described in [6, 14], and other stable solutions orbit the QP solutions in phase space. Since the amplitude scales out of the TTF, the QP solutions are described by “temperature” $T = E/N$; for fixed maximum mode number j_{max} , the maximum possible temperature is $d + 2j_{max}$. The QP solutions are special in that the time-dependence of each mode is harmonic, so QP solutions satisfy algebraic equations; [14] found low-temperature solutions to these equations directly. To reach higher temperatures, [14] perturbed low-temperature solutions by the addition of energy. Our main concern in this work is the persistence of QP solutions, especially those at high temperatures, as j_{max} increases since the full TTF theory takes $j_{max} \rightarrow \infty$.

**** LEFT THE REST ALONE, NEED TO DISCUSS ORGANIZATION AND METHODS WHEN WE’RE FINISHED

We show that high temperature QP solutions are very sensitive to truncation error and cannot be interpreted as physically relevant solutions. We then examine the time evolution of large j_{max} QP solutions at all temperatures in both the perturbative theory and the full, nonlinear theory. **[OTHER MAJOR GOALS HERE]**

This work is organized as follows: we begin in §3.3 with a review of the linearized solutions for a minimally coupled, massless scalar field in AdS_{d+1} and establish the renormalization flow equations that govern the time evolution of the amplitude and phase functions in the scalar field. In §3.4, we find quasi-periodic solutions in AdS_4 by directly solving a set of algebraic equations, and discuss the viability of reaching new QP solutions through repeated application of a perturbative scheme. We then examine the time evolution of a wide range of QP solutions in §3.5 in both the linearized theory and the full, nonlinear system. We end with a discussion in §3.6.

3.3 Minimally Coupled Scalar Fields in AdS_{d+1}

Consider a spherically-symmetric, asymptotically AdS_{d+1} spacetime with characteristic curvature ℓ . Written in Schwarzschild-like coordinates, the metric in units of AdS scale is given by

$$ds^2 = \frac{1}{\cos^2(x)} \left(-Ae^{-2\delta} dt^2 + A^{-1} dx^2 + \sin^2(x) d\Omega^{d-1} \right), \quad (3.1)$$

where the radius $x \in [0, \pi/2]$ and $-\infty < t < \infty$. A minimally-coupled, massless scalar field $\phi(t, x)$ is subject to the following Einstein and Klein-Gordon equations:

$$G_{ab} + \Lambda g_{ab} = 8\pi \left(\nabla_a \phi \nabla_b \phi - \frac{1}{2} g_{ab} (\nabla \phi)^2 \right) \quad (3.2)$$

$$0 = \frac{1}{\sqrt{-g}} \partial_a \sqrt{-g} g^{ab} \partial_b \phi. \quad (3.3)$$

The canonical equations of motion for the scalar field are

$$\partial_t \phi = Ae^{-\delta} \Pi, \quad \partial_t \Phi = \partial_x (Ae^{-\delta} \Pi), \quad \text{and} \quad \partial_t \Pi = \frac{\partial_x (\Phi Ae^{-\delta} \tan^{d-1}(x))}{\tan^{d-1}(x)}, \quad (3.4)$$

where the canonical momentum is $\Pi(t, x) = A^{-1} e^\delta \phi$ and $\Phi(t, x) \equiv \partial_x \phi$ is an auxiliary variable. In terms of these fields, (3.2)-(3.3) reduce to

$$\partial_x \delta = -(\Pi^2 + \Phi^2) \sin(x) \cos(x), \quad (3.5)$$

$$\partial_x A = \frac{d-2+2\sin^2(x)}{\sin(x) \cos(x)} (1-A) - A \sin(x) \cos(x) (\Pi^2 + \Phi^2). \quad (3.6)$$

3.3.1 Linearized Solutions

The linearized scalar field solutions come from expanding in terms of a small amplitude

$$\phi(t, x) = \sum_{j=0}^{\infty} \epsilon^{2j+1} \phi_{2j+1}(t, x), \quad A(t, x) = 1 - \sum_{j=1}^{\infty} \epsilon^{2j} A_{2j}(t, x), \quad \delta(t, x) = \sum_{j=1}^{\infty} \epsilon^{2j} \delta_{2j}(t, x). \quad (3.7)$$

Under this expansion, the $\mathcal{O}(\epsilon)$ terms give the linearized equation of motion for the scalar field:

$$\partial_t^2 \phi_1 + \hat{L} \phi_1 = 0 \quad \text{where} \quad \hat{L}_1 \equiv -\frac{1}{\tan^{d-1}(x)} \partial_x (\tan^{d-1}(x) \partial_x). \quad (3.8)$$

The eigenvalues of \hat{L} are simply $\omega_j^2 = (d+2j)^2$ and the eigenfunctions are

$$e_j(x) = k_j \cos^d(x) P_j^{(\frac{d}{2}-1, \frac{d}{2})}(\cos(2x)) \quad \text{with} \quad k_j = \frac{2\sqrt{j!(j+d-1)!}}{\Gamma(j+\frac{d}{2})}. \quad (3.9)$$

Note the the normalizations are chosen such that $\hat{L}e_j = \omega_j^2 e_j$ and

$$\langle e_i | e_j \rangle \equiv \int_0^{\frac{\pi}{2}} dx \bar{e}_i e_j \tan^{d-1}(x). \quad (3.10)$$

By expanding the scalar field functions in terms of the eigenbasis given in (3.9) and substituting into (3.8), we find that the time-dependent functions $c_n^{(2j+1)}(t) = \langle \phi_{2j+1}(t, x), e_n(x) \rangle$ satisfy $\ddot{c}_j^{(1)} + \omega_j^2 c_j^{(1)} = 0$. The general solution for the scalar field is can then be written in terms of time-dependent amplitude and phase variables:

$$\phi_1(t, x) = \sum_{j=0}^{\infty} A_j(t) \cos(\omega_j t + B_j(t)) e_j(x). \quad (3.11)$$

As discussed in [7, 11, 15], the integer nature of the mode frequencies mean that the spectrum is fully resonant. Unlike solutions such as oscillons, the resonant terms cannot be absorbed by a frequency shift and therefore result in *secular* terms: resonant contributions that grow rapidly with time and induce collapse. These resonant terms appear at $\mathcal{O}(\epsilon^3)$ and can be expressed in terms of a source, $S(t)$:

$$\ddot{\phi}_3 + \hat{L}\phi_3 = S \equiv 2(A_2 - \delta_2)\ddot{\phi}_1 + (\dot{A}_2 - \dot{\delta}_2)\dot{\phi}_1 + (A'_2 - \delta'_2)\phi'_1, \quad (3.12)$$

where A_2, δ_2 are the leading-order contributions to the metric functions in (3.7) that are determined by the $\mathcal{O}(\epsilon^2)$ backreaction with the metric. Projecting onto the $e_j(x)$ basis, the source term (*i.e.*, resonant contributions) can be expressed in terms of the time-dependent coefficients

$$\ddot{c}_j^{(3)} + \omega_j^2 c_j^{(3)} = S_j. \quad (3.13)$$

To control the growth of secular terms, [11] used resummation techniques to absorb singular contributions into the amplitude A_j and phase B_j of (3.11). This also resulted in a set of conserved quantities: the energy of the system, E , and particle number, N . The simultaneous conservation of both E and N implied that weakly turbulent systems exhibit dual cascades of energy, providing a mechanism through which two-mode data could remain stable [10].

3.3.2 Two-Time Formalism

The Two-Time Formalism (TTF) describes the solution to (3.8) in terms of slowly-modulating amplitude and phase variables, A_j and B_j , that are functions of the slow time $\tau = \epsilon^2 t$,

$$\phi(t, x) = \epsilon \sum_{j=0}^{\infty} A_j(\epsilon^2 t) \cos(\omega_j t + B_j(\epsilon^2 t)) e_j(x). \quad (3.14)$$

The next non-trivial order in the equations of motion include gravitational self-interactions of the scalar field, and provides source terms for A_j and B_j . Following the time-averaging procedure of [7] – and using the resonance condition $\omega_i + \omega_j = \omega_k + \omega_l$ to eliminate one of the indices – the l^{th} amplitude and phase are given by

$$-\frac{2\omega_l}{\epsilon^2} \frac{dA_l}{dt} = \sum_{i \neq l} \sum_{j \neq l}^{l \leq i+j} S_{ij(i+j-l)l} A_i A_j A_{i+j-l} \sin(B_l + B_{i+j-l} - B_i - B_j), \quad (3.15)$$

$$\begin{aligned} -\frac{2\omega_l A_l}{\epsilon^2} \frac{dB_l}{dt} &= T_l A_l^3 + \sum_{i \neq l} R_{il} A_i^2 A_l \\ &+ \sum_{i \neq l} \sum_{j \neq l}^{l \leq i+j} S_{ij(i+j-l)l} A_i A_j A_{i+j-l} \cos(B_l + B_{i+j-l} - B_i - B_j). \end{aligned} \quad (3.16)$$

The coefficients T, R, S are calculated directly from integrals over the product of eigenmodes and contain some useful symmetry properties: the integrals vanish except with the resonance condition $\omega_i + \omega_j = \omega_l$ is met.

Computationally, we find it more convenient to write T, R, S in terms of auxiliary coefficients with greater symmetry properties (as shown in [15]). The explicit expressions for these integrals in the interior gauge, in which $\delta(t, x = 0) = 0$, are given in appendix 3.B.

Using a complex amplitude of the form $\mathcal{A}_j(\tau) = A_j \exp(-iB_j)$ in (3.14) allows us to combine equations (3.15) and (3.16) into a single TTF equation:

$$-2i\omega_l \frac{A_l}{d\tau} = T_l |\mathcal{A}_l|^2 \mathcal{A}_l + \sum_{i \neq l} R_{il} |\mathcal{A}_i|^2 \mathcal{A}_l + \sum_{i \neq l} \sum_{j \neq l}^{l \leq i+j} S_{ij(i+j-l)l} \mathcal{A}_i \mathcal{A}_j \bar{\mathcal{A}}_{i+j-l}. \quad (3.17)$$

3.4 Quasi-periodic Solutions in AdS_4

The stability of the solutions to (3.17) can be examined using a *quasi-periodic* (QP) ansatz for the complex amplitude,

$$\mathcal{A}_j = \alpha_j e^{i\beta_j \tau}, \quad (3.18)$$

where $\alpha_j, \beta_j \in \mathbb{R}$. Substituting (3.18) into (3.14) allows us to relate the QP modes α_j and β_j to the amplitude/phase modes via $A_j = 2\alpha_j$, $B_j = \beta_j \tau$. When we examine how well the QP solutions solve the Einstein equations, we use this conversion to re-construct the scalar and metric fields from the QP solutions. The time dependence in (3.17) is removed via the condition $\beta_j = \beta_0 + j(\beta_1 - \beta_0)$, leaving β_0 and β_1 as unknown parameters. Considering modes of (3.14) up to some j_{max} , the QP ansatz results in a set of $j_{max} + 1$ algebraic equations for $j_{max} + 3$ unknowns

$$2\omega_l \alpha_l \beta_l = T_l \alpha_l^3 + \sum_{i \neq l} R_{il} \alpha_i^2 \alpha_l + \sum_{i \neq l} \sum_{j \neq l}^{l \leq i+j} S_{ij(i+j-l)l} \alpha_i \alpha_j \alpha_{i+j-l}. \quad (3.19)$$

As shown in [14, 17], the TTF is invariant under a $U(1)$ transformation that leads to the conserved quantities

$$E = 4 \sum_j \omega_j^2 \alpha_j^2 \quad \text{and} \quad N = 4 \sum_j \omega_j \alpha_j^2. \quad (3.20)$$

These definitions allow for two of the free parameters to be fixed. Families of solutions can be examined by fixing $\alpha_0 = 1$ and sampling a range of α_1 values in the range $\alpha_1 \ll \alpha_0$. The families of solutions can be distinguished by their “temperature”, or energy per particle number $T = E/N$.

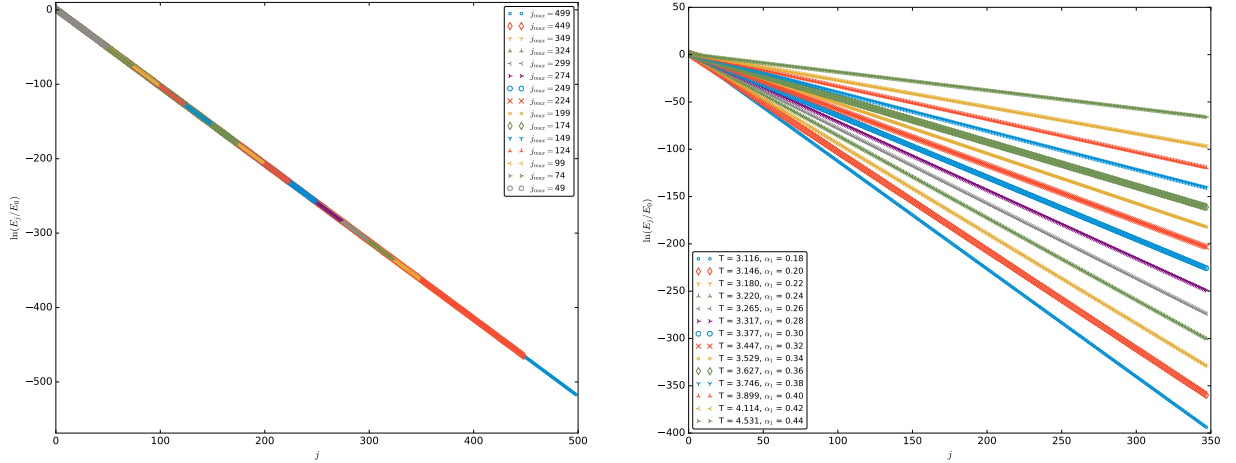
Practically speaking, finding solutions to the j_{max} equations that arise from (3.17) requires truncating the series at a finite value $j_{max} < \infty$. These solutions must continue to be present and unaffected by increasing j_{max} to represent true solutions to the perturbative system.

3.4.1 Persistence at Large j_{max}

The question of edge effects in determining the stability of a particular solution is important to investigate. For instance, if a particular solution to (3.19) is found for some α_1 when $j_{max} = 50$,

does this continue to be a solution when we consider more modes, say $j_{max} = 250$? By following the methods outlined in appendix 3.A, we are able to start with a low j_{max} solution and incrementally increase the number of modes being considered up to several hundred. This method was found to be more successful, given the optimization algorithms being used, than other seeding methods.

As an example, consider solutions to (3.19) with the conditions $\alpha_0 = 1.0$ (since all QP solutions are defined up to an overall scale, $\alpha_0 = 1.0$ is taken to always be true) and $\alpha_1 = 0.2$, which corresponds to an initial temperature of $T_0 \simeq 3.146$. In figure 3.1a, we present an overlay of QP solutions generated by successive solving, fitting, and seeding from $j_{max} = 50$ to $j_{max} = 500$ for two families of QP solutions. Similar high j_{max} solutions were confirmed for $\alpha_1 \leq 0.442$.



(a) An overlay of QP solutions with $\alpha_1 = 0.2$, corresponding to $T_0 \simeq 3.146$.

(b) QP solutions up to $j_{max} = 350$.

Figure 3.1: Energy spectra for various QP solutions.

When examining the range of α_1 values that result in QP solutions existing, it was found that any solution that existed at small j_{max} could be extended to large j_{max} with proper seeding and sufficient computing power. However, a hard limit exists at the maximum α_1 value of $\alpha_1 = 0.442$, corresponding to a temperature of $T \simeq 4.643$. Above this limit, no QP solutions can be found even for j_{max} values as low as $j_{max} = 50$. There seem to be no solutions that exist at low j_{max} that cease to exist at high j_{max} . Furthermore, there is no corresponding lower limit to α_1 values; as $\alpha_1 \rightarrow 0$ with $\alpha_j > \alpha_{j+1}$, the TTF solution approaches the well-known single-mode solution.

3.4.2 High Temperature Perturbations

In [14], additional QP solutions can be found by repeatedly perturbing existing solutions. The addition of some energy δE corresponds to the changes $\alpha_j \rightarrow \alpha_j + u_j$ and $\beta_j \rightarrow \beta_j + \theta_1 + \omega_j \theta_2$. The

perturbed quantities are given by the system of *linear* equations

$$\delta E = 4 \sum_j \omega_j^2 \alpha_j u_j \quad (3.21)$$

$$\delta N = 4 \sum_j \omega_j \alpha_j u_j = 0 \quad (3.22)$$

$$\begin{aligned} 0 = & \omega_l (\alpha_l (\theta_1 + \omega_l \theta_2) + \beta_l u_l) + 6 T_l \alpha_l^2 u_l + 2 \sum_{i \neq l} R_{il} (\alpha_i^2 u_l + 2 \alpha_i \alpha_l u_l) \\ & + 2 \sum_{i \neq l} \sum_{j \neq l}^{l \leq i+j} S_{ij(i+j-l)l} [u_i \alpha_j \alpha_{i+j-l} + u_j \alpha_i \alpha_{i+j-l} + \alpha_i \alpha_j u_{i+j-l}]. \end{aligned} \quad (3.23)$$

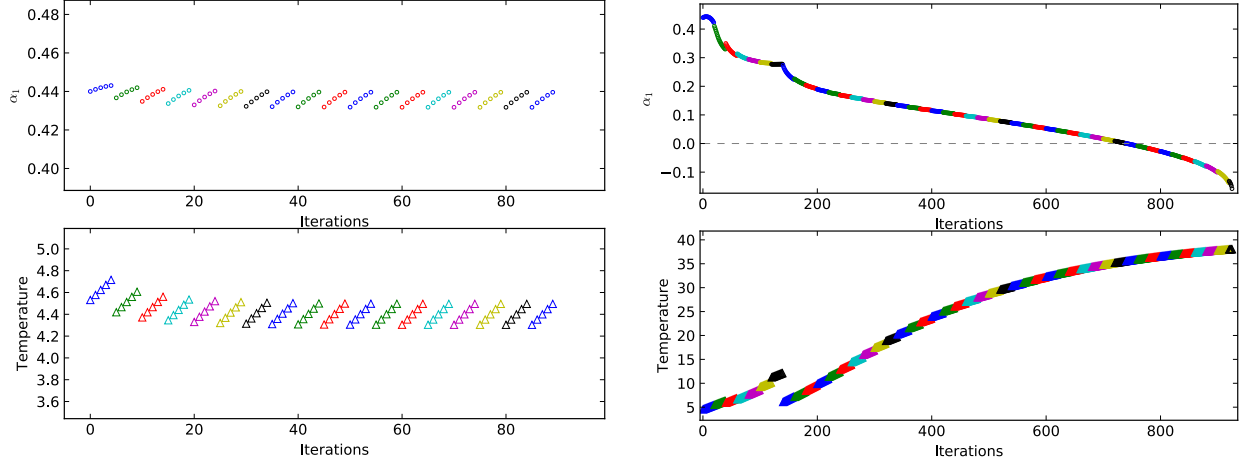
Therefore, by solving (3.21)-(3.23) for $\{u_j, \theta_1, \theta_2\}$, the existing QP solution can be updated and the process can be repeated.

For a standard QP solution with $\alpha_1 = 0.2$, the initial temperature is $T_0 = 3.146$. By applying the high temperature perturbation method described above, we are able to increase the temperature of the solution. However, this process must be examined with some scrutiny; applying repeated perturbations to a known solution does not guarantee the final result remains a valid solution. To investigate this further, we have implemented a solver that projects back down to the QP solution plane after either a set number of perturbations, or after every perturbation. When a solution can no longer be projected back to the QP plane, we have perturbed too far and the state no longer represents a quasi-periodic TTF solution.

Consider figure 3.2. When the result of the linear perturbations is projected back down to the QP plane every 5 iterations, we see that the solution approaches an attractor and is unable to accumulate enough energy to escape this local minimum before being projected back down to the QP plane. However, when the projection frequency is decreased to every 20 iterations, the attractor solution is able to be bypassed; note that as the iteration number increases, we actually see a *decrease* in α_1 value while the temperature continues to increase. At iteration 150 in figure 3.2b, there is a cusp in α_1 and a corresponding drop in temperature. Moreover, α_1 becomes negative after several hundred iterations.

Let us examine the energy spectra of the solutions shown in figure 3.3a. When projecting back to the QP plane every 5 perturbations, the energy spectra do not deviate far from the initial solution; however, no temperature increase is observed. We denote solutions found by this method as “threshold temperature” solutions. The threshold temperature T_{th} is robust against increases in j_{max} and therefore is independent of edge effects. See table 3.1 for further details.

When the projection frequency is decreased to 20 iterations an increase in temperature can be observed, as seen in figure 3.3b. However, the discontinuous behaviour of the temperature as a function of iteration is a signal of the energy spectrum losing its smooth profile (*c.f.* spectra of iterations 120 and 180). This in itself is not necessarily a breakdown of the quasi-periodic nature of the solution. Upon examining the condition number of the matrix formed by (3.21)-(3.23), we find that in fact the problem becomes ill-conditioned. This results in a absolute value of u_i that is greater than α_i ; that is, the perturbative condition required to derive the system of linear equations (3.21)-(3.23) breaks down. For many prospective high-temperature solutions, this break-down of the perturbative condition is signalled by the development of spikes in the energy spectra caused by the values of α_j becoming negative. In § 3.5.2.1 we will examine the effects of using such solutions as initial data in the evolution of the QP solution.



(a) The result of applying repeated iterations of the linear perturbations to the initial QP solution of $\alpha_1 = 0.44$, projecting back to the QP plane every five iterations. The perturbation amount (δE in (3.21)) is fixed to 1% of the initial energy.

(b) Starting from the same $\alpha_1 = 0.44$ QP solution, linear perturbations are again applied, this time projecting back to the QP plane every 20 iterations.

Figure 3.2: The results of projecting a $j_{max} = 50$, $\alpha_1 = 0.44$ solution back to the QP plane at various frequencies during high temperature perturbations. Colour changes indicate that the non-linear solver has been applied.

3.4.3 Building High-Temperature Solutions

Despite high-temperature solutions being inaccessible via repeated energy perturbations, we may ask if such solutions can be found by using different methods. First, we consider perturbing a known QP solution to a high temperature *without* regular projections back to the QP plane. Then, at some sufficiently high temperature T_{max} , we attempt to project back to the QP plane. In figure 3.4a, the spectra of QP solutions before and after projection are shown for increasing j_{max} . For solutions with $j_{max} \geq 100$, high-temperature solutions are in fact projected to low-temperature solutions that may contain negative α_j values. Low- j_{max} solutions, however, appear to remain at high-temperatures after projecting back to the plane. We use this type of solution in our next method.

Starting with a low- j_{max} , high-temperature solution, we can use a fitting procedure similar to that used to find high- j_{max} , quasi-periodic solutions in §3.4.1. Instead of fitting α_j values away from the highest modes, we instead apply the tail fitting the final 5 modes and use the fit to generate seed values for a $j_{max} + 5$ solution. We see in figure 3.4b that this method results in spectra where energy becomes increasingly concentrated in high- j modes. In fact, for solutions with $j_{max} \geq 90$, and equal or greater amount of energy resides in the high- j modes than in the zero-mode. Intuitively, such a solution would collapse very quickly in the full system due to the high concentration of energy on small length scales. However, because we have arrived at this solution through the two-time formalism, evolution using (3.15)-(3.16) would ensure the solutions remain stable. To help quantify the stability of QP solutions against collapse, we calculate the scalar curvature at the origin.

j_{max}	T_{th}	Iterations
50	4.30344575697724e+00	350
75	4.30344544264076e+00	210
100	4.30344544023857e+00	540
150	4.30344544024198e+00	280
200	4.30344544023915e+00	300

Table 3.1: Values of the threshold temperature T_{th} for QP solutions with given j_{max} . Also included is the number of iterations applied (projecting back to the solution plane after every five iterations).

3.4.4 Stability of QP Solutions

3.4.4.1 The Ricci Scalar at the Origin

While the TTF theory itself is stable by construction, we can examine the behaviour of the Ricci scalar at the origin for indications that collapse might occur in the full, nonlinear system. Large values or rapid increases in the Ricci curvature at the origin often indicates impending collapse (ref?) in numerical simulations. Therefore, we use increases in scalar curvature as a potential indication of collapse. In figure 3.5, we show the highly oscillatory behaviour of the Ricci scalar corresponding to the $T \simeq 66.6$ high-temperature solution presented in figure 3.4b. Note that the upper envelope of Π^2 is $\mathcal{O}(10^{12})$ immediately; this suggests that the high-temperature solution is *not stable* against collapse, even on perturbative timescales. Conversely, the constant behaviour and maximum amplitude $\mathcal{O}(10^4)$ of Π^2 for the $T \simeq 3.15$ QP solution – over multiples of the perturbative timescale – confirms that the solution remains quasi-periodic and does not collapse.

3.4.4.2 Constraint Equations

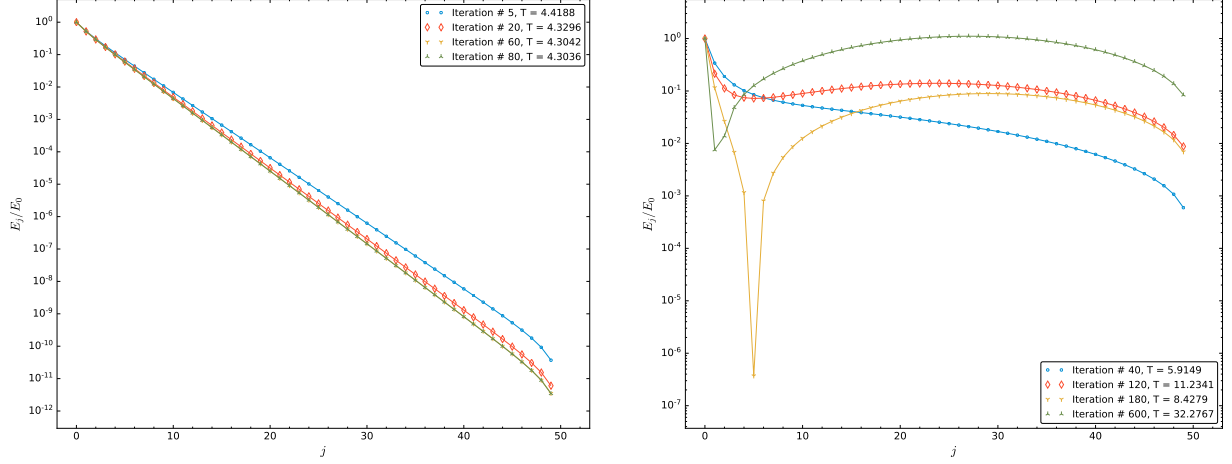
Another indicator of possible collapse and/or violation of the perturbative approximation is the growth of residuals when the TTF solutions are substituted into the Einstein equations. The residuals are calculated by reconstructing the time dependence of the scalar field and its derivatives using the amplitude-phase variables, and comparing the $\mathcal{O}(\epsilon^2)$ values of the derivatives of the metric functions in (3.5)-(3.6). In particular, using the numerical values of the amplitude-phase variables A_j and B_j , (3.11) gives the value of the leading-order scalar field contribution, $\phi_1(t, x)$. The $\mathcal{O}(\epsilon^2)$ contribution to the derivatives of metric functions come from

$$\partial_x \delta_2(t, x) = -\sin(x) \cos(x) \left((\partial_x \phi_1)^2 + (\partial_t \phi_1)^2 \right), \quad (3.24)$$

$$\partial_x A_2(t, x) = -\frac{1 - d + \cos(2x)}{\sin(x) \cos(x)} (A_2 - 1) - \sin(x) \cos(x) \left((\partial_x \phi_1)^2 + (\partial_t \phi_1)^2 \right), \quad (3.25)$$

$$\text{with } A_2(t, x) = -\frac{\cos^d(x)}{\sin^{d-1}(x)} \int_0^x \tan^{d-1}(y) \left((\partial_t \phi_1)^2 + (\partial_x \phi_1)^2 \right) dy. \quad (3.26)$$

The L^2 -norm of the differences between (3.24)-(3.25) and (3.5)-(3.6) would constitute the residuals of the Einstein equations. However, while the leading-order contribution to the residuals is $\mathcal{O}(\epsilon^4)$,



(a) Energy spectra when projecting back to the QP solution plane every 5 iterations for an initial $\alpha_1 = 0.44$, QP solution (see figure 3.2a for temperature and α_1 as a function of iteration). (b) The same initial QP solution as figure 3.3a is used, but is projected back to the QP plane every 20 iterations.

Figure 3.3: Comparing energy spectra of high-temperature perturbations of an $\alpha_1 = 0.44$ QP solution that have been projected back to the QP plane at different frequencies.

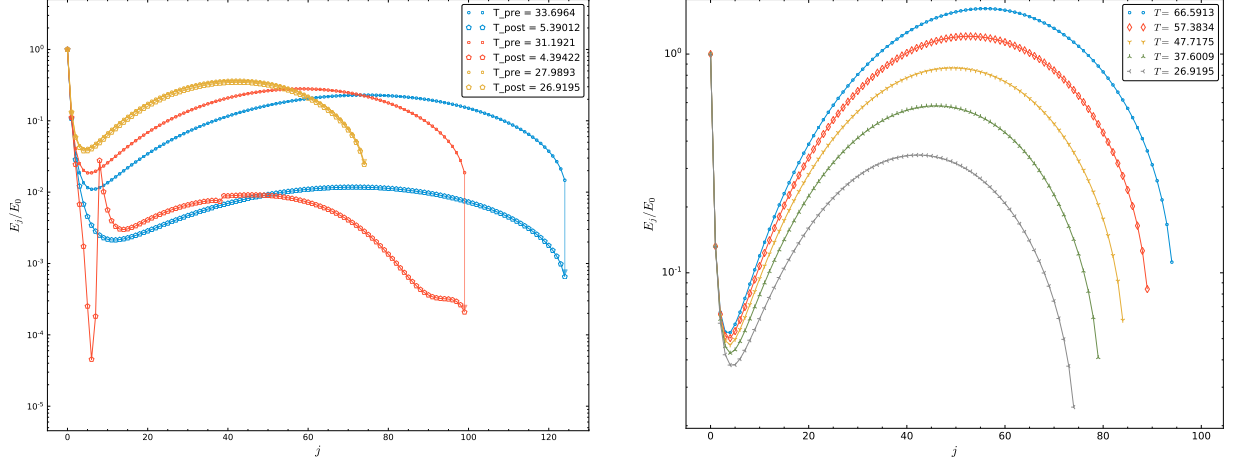
there are in fact higher order terms that enter into the calculation of $\partial_t \phi$. A careful evaluation of the constraints would therefore include calculating the $\mathcal{O}(\epsilon^4)$ term in the metric function $A(t, x)$ so that the product $A(\Phi^2 + \Pi^2)$ would include terms $\mathcal{O}(\epsilon^6)$. Instead, we limit our focus to examining only the difference between (3.5) and (3.24), which does not suffer from higher-order contributions. The examination of residuals is taken as a suggestion of how well a TTF solution continues to satisfy the Einstein equations throughout its evolution. In figure 3.6, we show the absolute and relative L^2 -norms both QP and high temperature solutions.

3.5 Time Evolution of Quasi-Periodic Solutions

Using the numerical evolution methods from [24], we use a variety of quasi-periodic and high-temperature solutions discussed above as initial data. We then examine their evolution under (3.15)-(3.16).

For each type of solution below, we can generate the following plots:

- Ricci scalar at the origin
- Einstein equation residuals
- Energy spectra (mode evolution, full spectrum evolution)
- QP equation residuals
- Projection of amp/phase intermediate solutions back to QP plane



(a) QP solutions perturbed to $T_{\text{max}} = 30.00$, which were then used as seeds for the nonlinear solver. Arrows are oriented from pre-optimized to post-optimized solutions. (b) Extensions of the $j_{\text{max}} = 50$ solution from figure 3.4a to larger j_{max} solutions using tail fitting on only the final 5 modes of the solution.

Figure 3.4: Constructing high temperature solutions “by hand.”

3.5.1 Quasi-Periodic Solutions

Consider first the evolution of a known QP solution. We see in figure 3.7 that the fraction of the total energy in the lowest- j modes remains constant over the duration of the evolution, while the fraction in the highest- j modes increases after $\tau \simeq 0.3$. Given the scale of the energy in the modes $j \geq 96$, this growth can mainly be attributed to numerical errors.

To better understand how well the QP solutions continue to satisfy the TTF equation throughout their time evolution, we evaluate the residuals of (3.19) using data taken during the evolution. Figure 3.8 is a sample of the L^2 -norm of these residuals using values for the amplitude-phase variables $A_j(\tau)$, $B_j(\tau)$ during evolution. We also examine changes in the spectrum during the evolution, and show that there is very little deviation between the initial and final spectra for QP solutions beyond numerical drift.

Furthermore, we can attempt to project the evolved solutions back to the QP plane at various times to explore if these solutions lose their quasi-periodic nature. We observe that the time-evolved, low-temperature QP solutions are easily projected back to the solution plane at all times during the evolution, and that the resulting solutions solve the QP equation (3.19) to a high degree of accuracy (see figure 3.9a). While this is to be expected for such low-temperature QP solutions, we will soon see that even padding a known QP solution with zeros causes the loss of quasi-periodicity during evolution. For comparison, figure 3.9b shows the results of attempting to project a QP solution that has been padded with zeros back to the QP plane during its evolution. Note the scale on the plot of the L^2 -norm in either case.

3.5.1.1 Padded QP Solutions

In an effort to extend the space of QP solutions, another method used to find solutions that exist nearby known QP solutions – but are not accessible through perturbative or conventional seeding

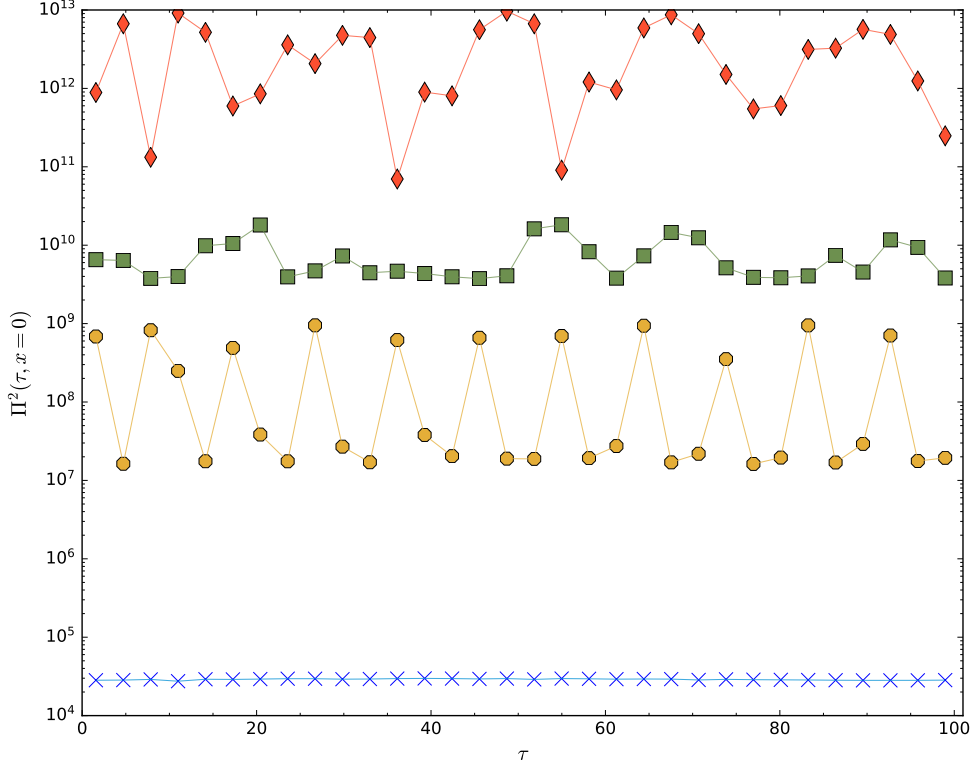
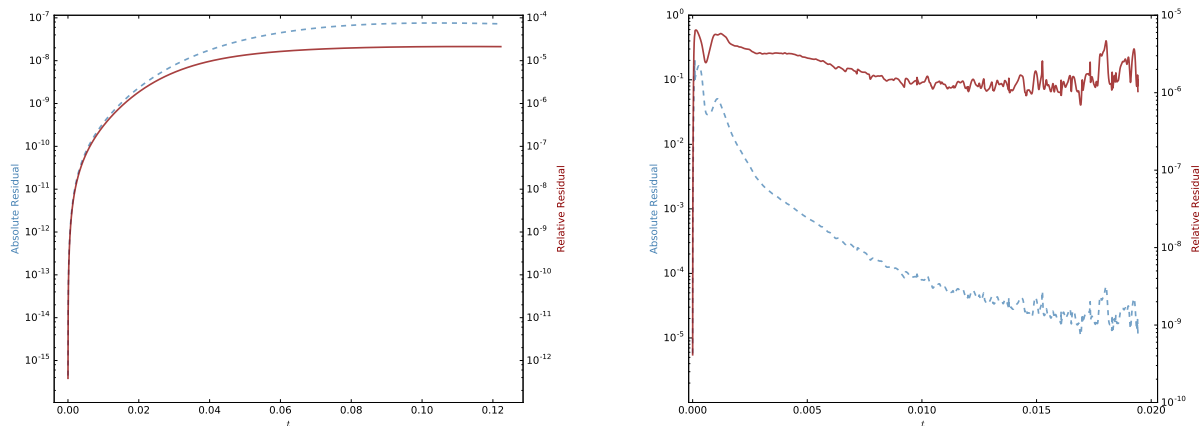


Figure 3.5: Comparing the upper envelope of Π^2 at the origin per light-crossing time for selected low- and high-temperature solutions with $\epsilon = 1$: $j_{max} = 375$, QP $T \simeq 3.15$ (blue crosses); $j_{max} = 75$, high-temperature $T \simeq 26.9$ (yellow octagons); $j_{max} = 100$, high temperature $T \simeq 75.35$ (green squares); $j_{max} = 95$, high temperature $T \simeq 66.6$ (red diamonds).

methods – is to pad a given quasi-periodic solution with extra modes that are initially set to zero. Upon amplitude-phase evolution, the energy in the lower- j modes will flow into the higher- j modes and a new quasi-periodic solution may be found. In figure 3.10, we construct initial data out of a known $j_{max} = 100$, $T \simeq 3.14$ solution by padding with zeros up to $j_{max} = 200$. As in the case of unpadded QP solution, the fraction of the total energy in the first four modes does not vary during the evolution and the highest modes accumulate some numerical error before levelling off. In figure 3.10d, we see the accumulation of numerical error in the higher modes as the evolution progresses. Also included is the value of the Ricci scalar at the origin, and the residuals of the QP equation throughout the evolution.

Despite the somewhat normal profile of the spectra of padded QP solution, we see in figure 3.9b that intermediate solutions during the evolution in fact *do not* project back to the QP plane. Rather, as hinted at by the Einstein equation residuals shown in figure 3.10f, the solutions have drifted away from their quasi-periodic initial data. It remains to be seen whether such profiles would be stable in the fully nonlinear system.

Using a known QP solution, we may ask how far away from the solution plane we can move by padding with an incremental number of zeros. In figure 3.11, we show the result of using intermediate solutions from the amplitude/phase evolution of a $j_{max} = 100$ QP solution padded with only five modes (initially set to zero). Despite QP solutions existing for $j_{max} = 105$, no solution was found when using the padded solution – at any point in its evolution – as a seed.



(a) An $\alpha_1 = 0.44$, $j_{\max} = 100$ QP solution with $\epsilon = 0.001$. (b) A $j_{\max} = 100$, high-temperature solution is padded with zeros to $j_{\max} = 125$ and evolved with $\epsilon = 0.001$.

Figure 3.6: Residuals from evaluating the constraints for QP and high temperature solutions.

3.5.2 High-Temperature Solutions

High-temperature solutions are those that are found by repeated applications of energy perturbations described in § 3.4.2. These come in several varieties based on the methods used to obtain them; namely, the frequency of projection back to the QP solution plane versus constructing solutions “by hand.” Note that solutions obtained without projecting back to the QP plane, or via the threshold temperature method, *are not* robust in the limit of large j_{\max} (see Appendix 3.C for further discussion on the extension of high-temperature solutions to large j_{\max}). However, it will be useful nonetheless to contrast their behaviour with other high-temperature solutions.

3.5.2.1 Regular Projections to the QP Plane

Here we examine a high-temperature solution obtained from repeatedly adding small amounts of energy to a $j_{\max} = 100$, $\alpha_1 = 0.44$ QP solution. First, we consider threshold temperature solutions discussed in § 3.4.2 – those that are on the cusp of quasi-periodic data but cannot be found through solving (3.19) alone. See figure 3.12 for results.

Threshold temperature solutions behave much like low-temperature quasi-periodic solutions: no energy transfer occurs among the leading modes, while very little occurs in the highest modes. Note the scale in figure 3.12b. Unlike other QP solutions with similar total number of modes, the highest modes in threshold temperature solutions contain $\mathcal{O}(10^{-7})E_T$. This relatively high value of the fraction of the total energy means that numerical errors remain suppressed throughout the evolution.

3.5.2.2 “By Hand” High-Temperature Solutions

Following the method outlined in § 3.4.3, we consider high-temperature solutions constructed by hand out of lower j_{\max} solutions. We now examine the behaviour of one such solution under amplitude-phase evolution.

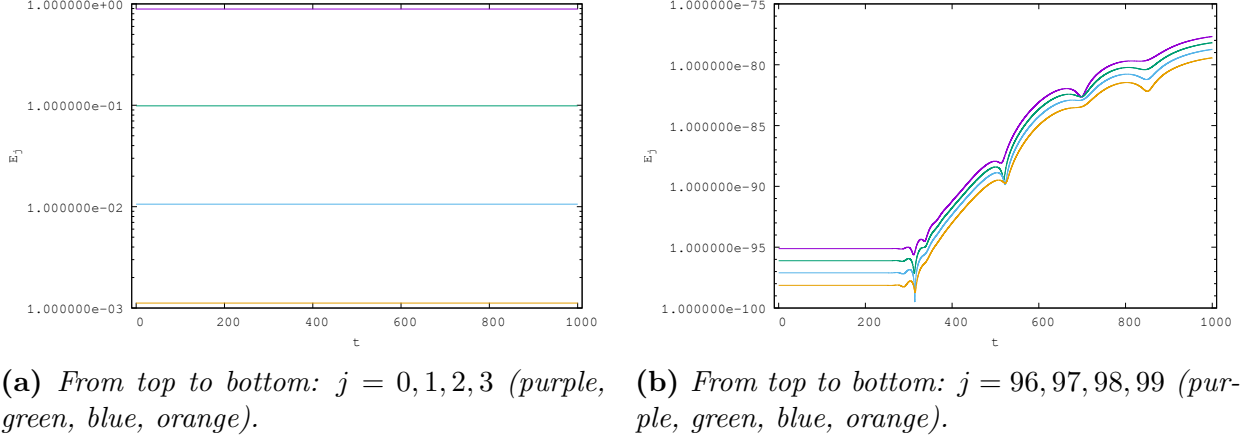


Figure 3.7: Amplitude-phase evolution of an $\alpha_1 = 0.2$, $j_{\max} = 100$, QP solution with $\epsilon = 0.01$. Similar behaviour is observed for higher j_{\max} solutions and over values of $0.2 \leq \alpha_1 \leq 0.44$.

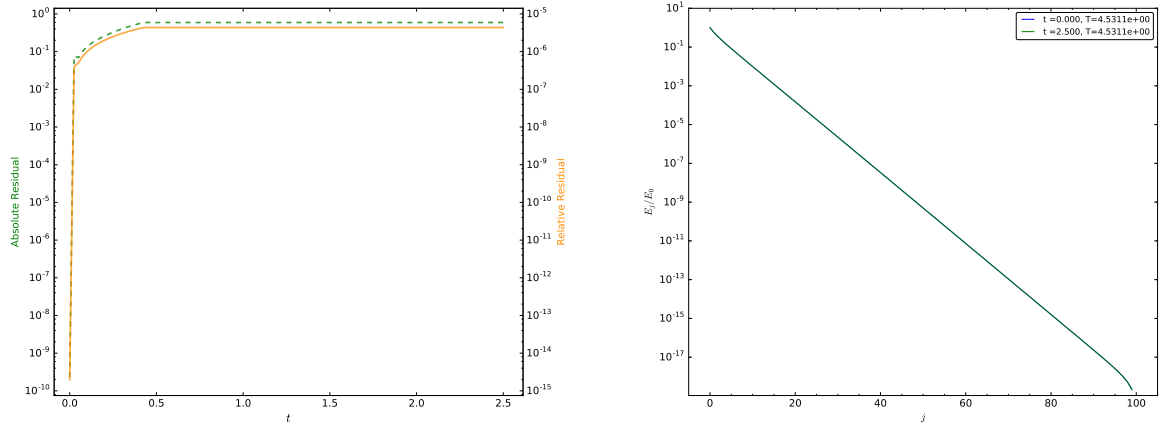


Figure 3.8: Left: L^2 -norm of the residuals of (3.19) evaluated at intervals of 0.025 during the evolution of a $j_{\max} = 100$, $\alpha_1 = 0.44$ QP solution with $\epsilon = 0.1$. Right: The spectra of the QP solution at the beginning and end of the evolution.

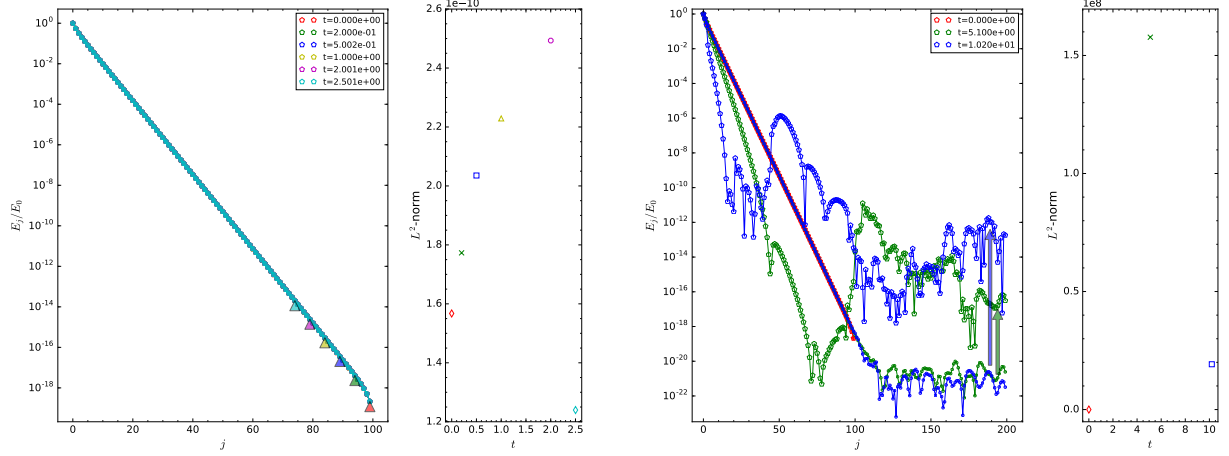
Attempt padding out to $j_{\max} = 125$ and run the evolution: see figure 3.14

Finally, consider padding such a solution out to $j_{\max} = 200$. See figure 3.15 for results.

The evolved profile of the high-temperature solution can no longer be projected back to the QP solution plane: figure 3.16.

3.5.2.3 Perturbing to an Intermediate Temperature Before Reoptimizing

Here, a QP solution is perturbed to a high temperature without regular projections back to the QP plane. At a pre-determined temperature cutoff, $T = 20.0$, the perturbation procedure is halted and the solution is used as a seed for the nonlinear solver. Instead of projecting to a QP solution at a high temperature, the nonlinear solver converges to a solution with only $T \sim 6.71$. We apply the amplitude-phase evolution procedure to the intermediate $T = 20.0$ solution in order to study how a solution for far away from the QP plane may behave. See figure 3.17 for results.



(a) Projected solutions for a low-temperature, QP solution and their L^2 -norms at $t \simeq 0.0, 0.2, 0.5, 1.0, 2.0, 2.5$ (red diamond, green cross, blue square, yellow triangle, magenta circle, blue diamond).

(b) The same QP solution is padded with zeros out to $j_{max} = 200$ and evolved in time. Intermediate solutions are projected back to the QP plane at $t \simeq 0.0, 5.1, 10.2, \dots$ (red diamond, green cross, blue square ...)

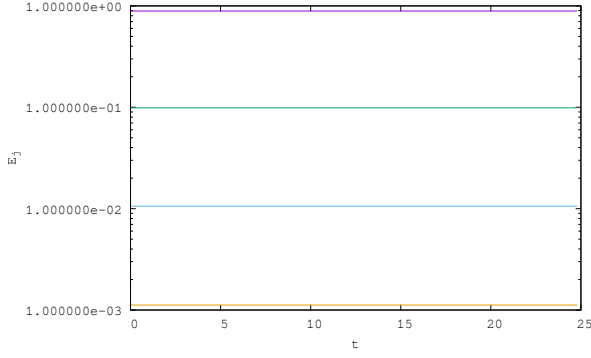
Figure 3.9: Intermediate values from the amplitude/phase evolution of a solution are used as seeds for the nonlinear solver at various times. Arrows are oriented from amplitude/phase seed values (circles) to QP plane projections (pentagons).

3.5.2.4 Padded Threshold Temperature Solutions

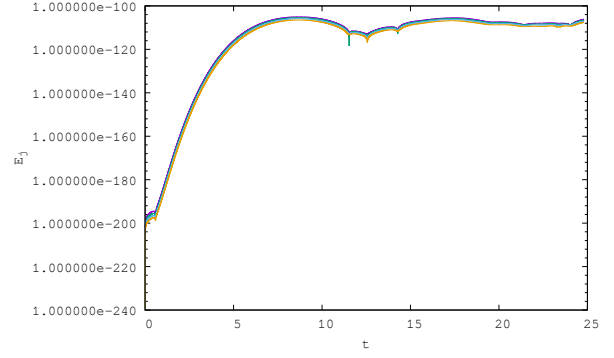
Padding the threshold temperature solution of $T \sim 5.4$ from $j_{max} = 100$ to $j_{max} = 200$ and then evolving in time produces very little change in the spectrum's profile. See figure 3.18 for results. Despite appearing to remain a high-temperature solution, the evolution of this profile renders it non-QP, as shown in figure 3.19. For a more concrete examination, figure 3.20 shows the threshold temperature solution for $j_{max} = 200$ as well as padded threshold solutions during their evolution. Under amplitude/phase evolution, the padded solution *does not* approach the known threshold solution.

3.6 Discussion

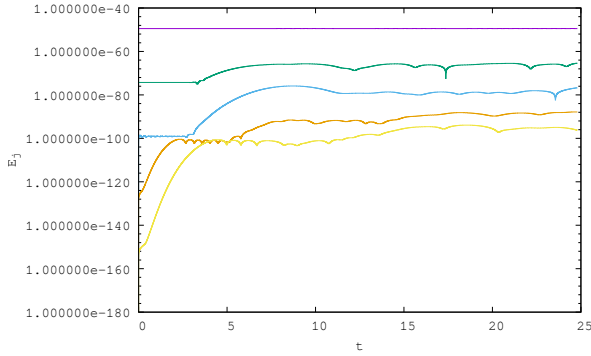
Acknowledgments The work of ND is supported in part by a Natural Sciences and Engineering Research Council of Canada PGS-D grant to ND, NSF Grant PHY-1606654 at Cornell University, and by a grant from the Sherman Fairchild Foundation. The work of BC and AF is supported by the Natural Sciences and Engineering Research Council of Canada Discovery Grant program. This research was enabled in part by support provided by WestGrid (www.westgrid.ca) and Compute Canada Calcul Canada (www.computecanada.ca).



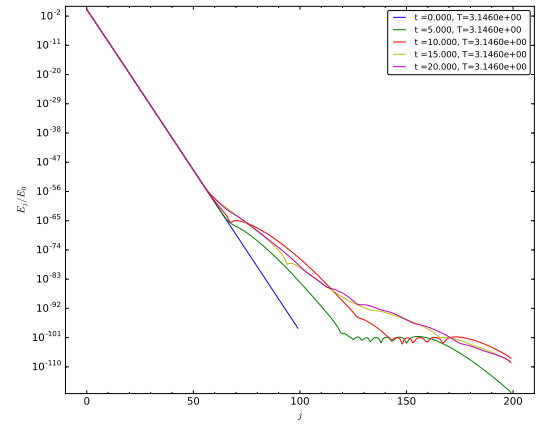
(a) The evolution of the first four modes of the padded QP solution: $j = 0, 1, 2, 3$ (purple, green, blue, orange).



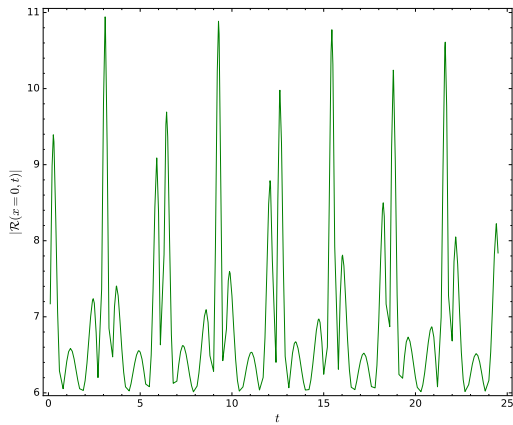
(b) The evolution of the last four modes: $j = 196, 197, 198, 199$ (purple, green, blue, orange).



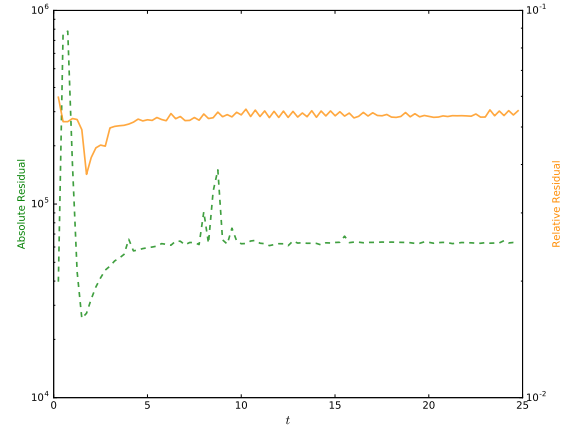
(c) Comparing the evolution of a selection of modes: $j = 50, 75, 100, 125, 150$ (purple, green, blue, orange, yellow).



(d) The total spectrum of the padded QP solution as a function of time.



(e) The Ricci scalar at the origin as a function of time for the padded QP solution.



(f) The residuals of the QP equation (3.19) throughout the amplitude-phase evolution of the padded QP solution.

Figure 3.10: The evolution of the padded QP solution for $\alpha_1 = 0.2$ and $j_{max} = 200$, with amplitude $\epsilon = 0.1$.

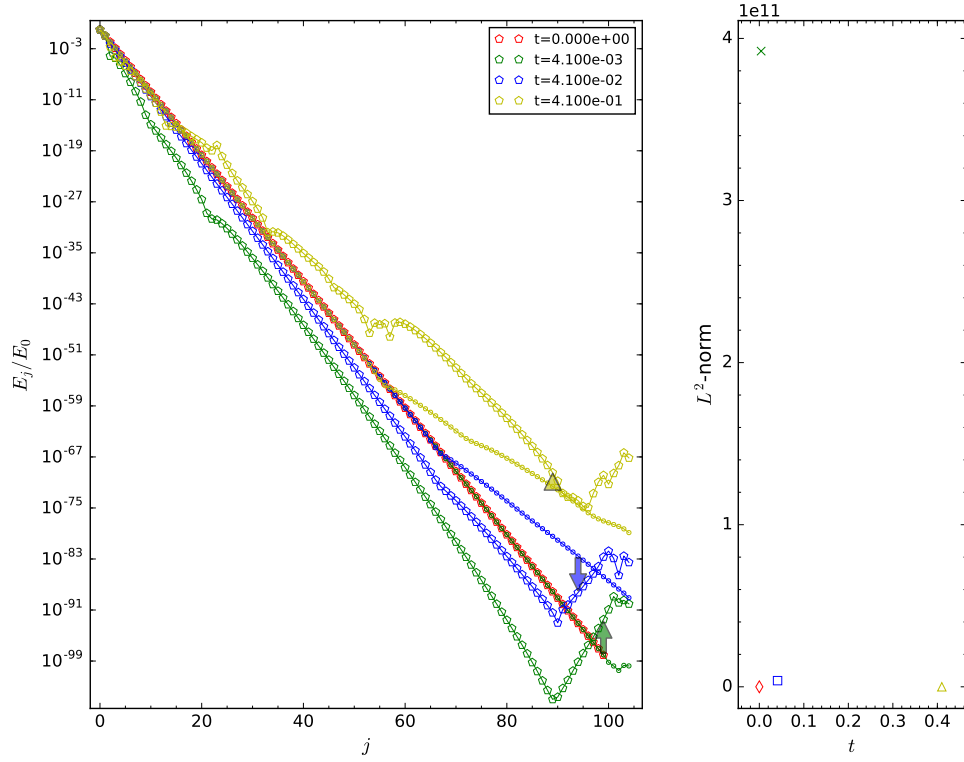
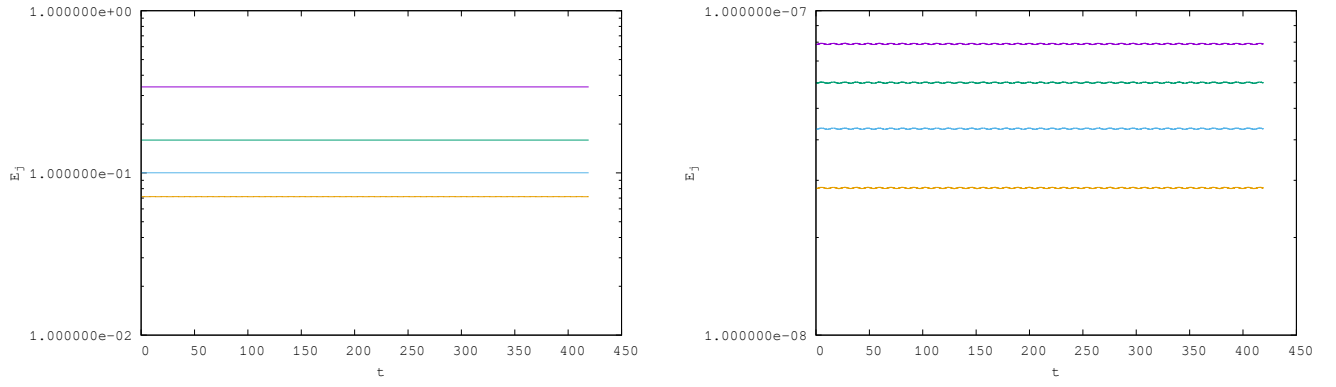


Figure 3.11: Left: Normalized spectra for a $j_{max} = 100$, QP solution that has been padded with five extra modes, then evolved in time. Intermediate spectra are used as seeds for projecting back to the QP plane at times $\tau \simeq 4.1 \times 10^{-3}$, 4.1×10^{-2} , 4.1×10^{-1} (green, blue, yellow). Arrows are oriented from seed spectra to best fit spectra. Right: Corresponding L^2 -norms of the error for each solution.



(a) $j = 0, 1, 2, 3$ (purple, green, blue, orange).

(b) $j = 96, 97, 98, 99$ (purple, green, blue, orange).

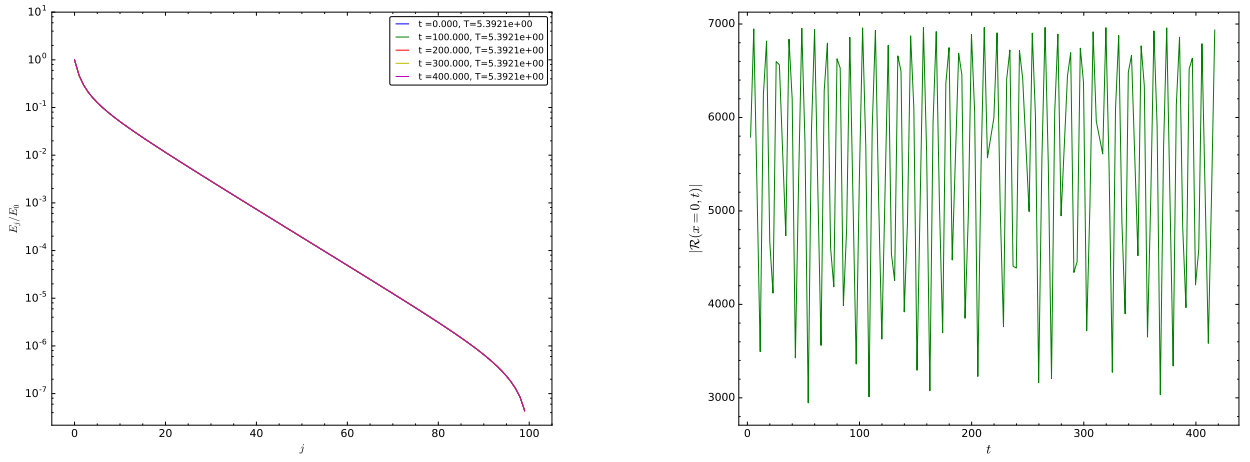


Figure 3.12: Above: The evolution the fraction of the total energy in specific modes for a $T \sim 5.4$, threshold temperature solution for $\tau \in [0, 4.25]$. Below: Snapshots of the full spectrum at various times in its evolution, as well as the upper envelope of $|R(t, x=0)|$ when $\epsilon = 0.1$.

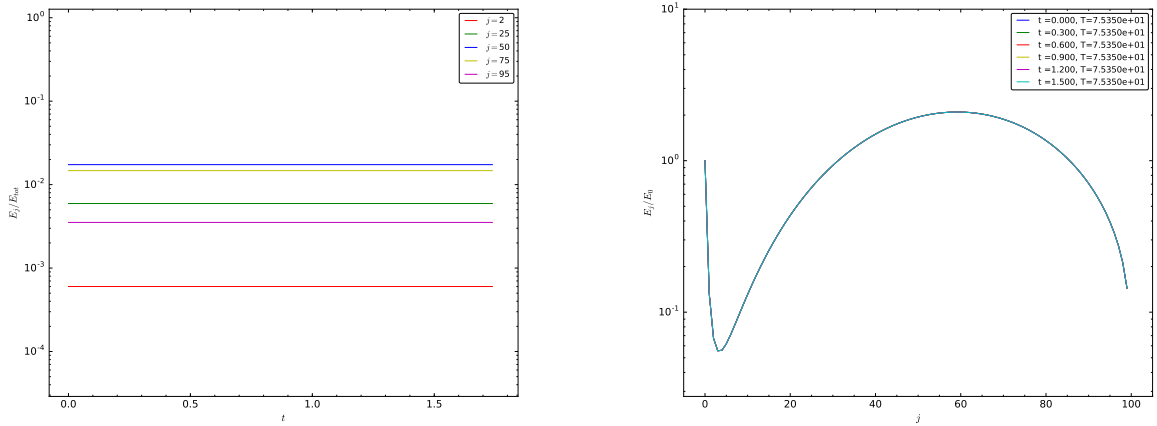


Figure 3.13: The evolution of a high-temperature solution created by hand from lower j_{max} solutions.

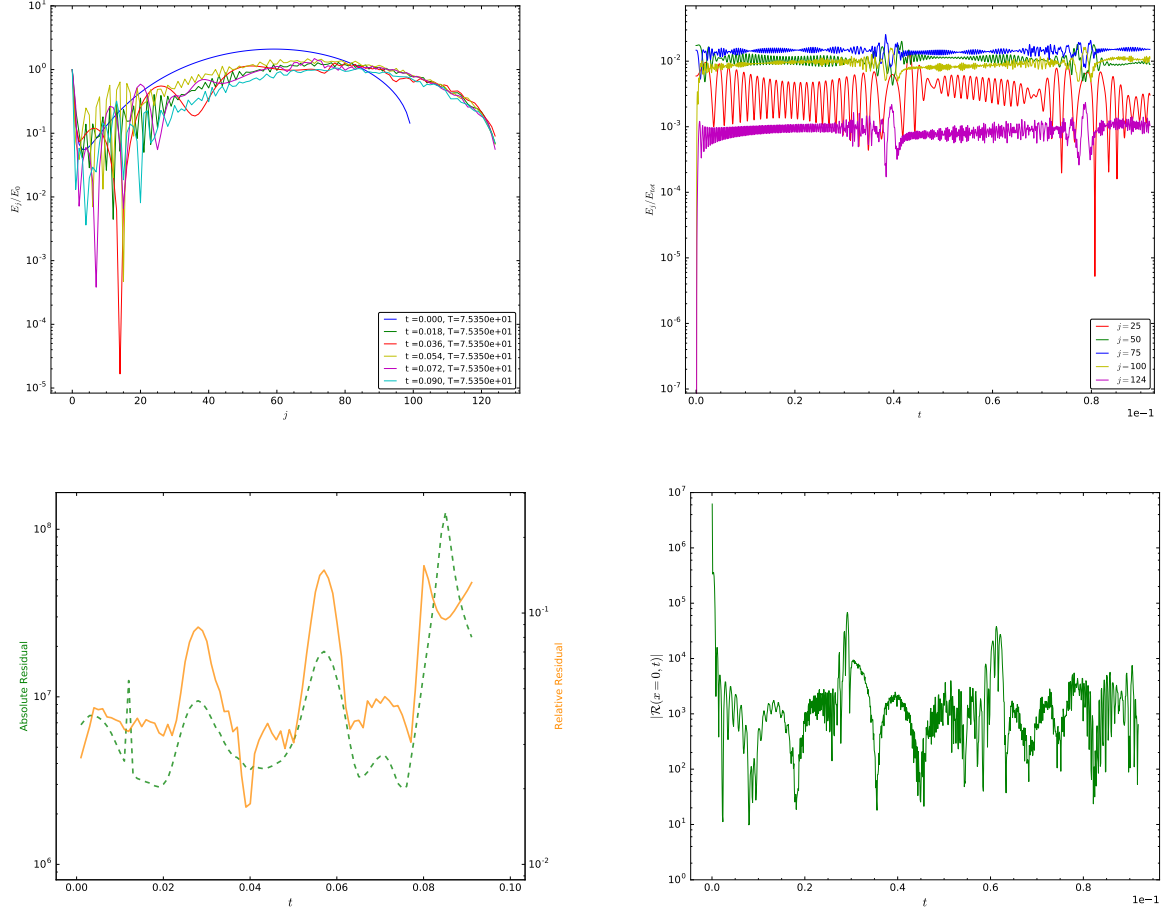


Figure 3.14: *Padding the same initial solution from figure 3.4, but with only 25 extra modes.*

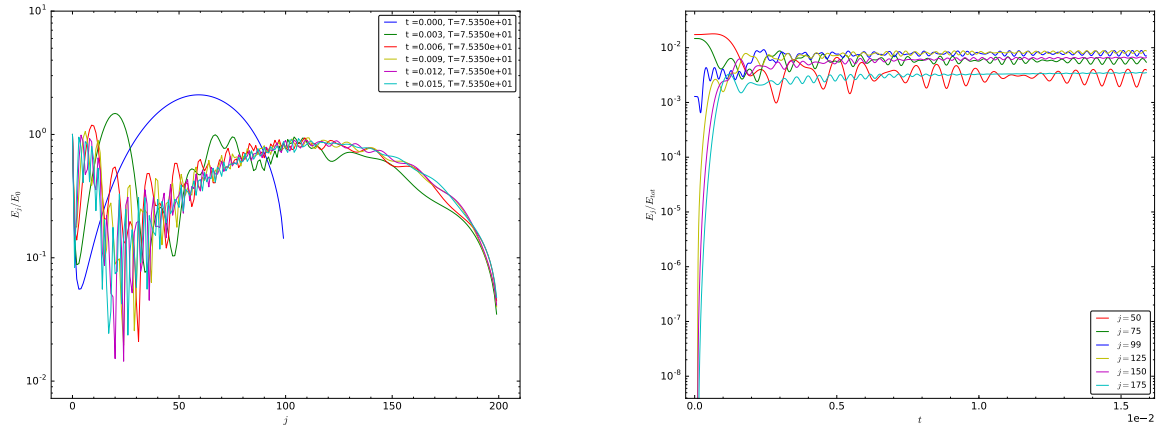


Figure 3.15: *Padding a $j_{max} = 100$, high temperature solution to $j_{max} = 200$ and evolving in time. $\epsilon = 0.1$*

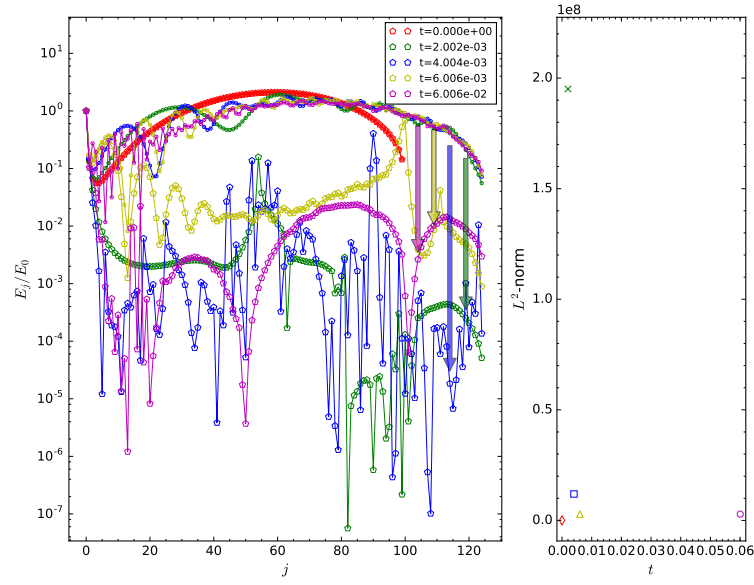
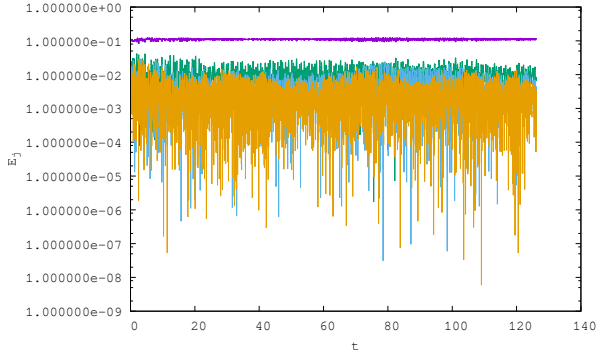
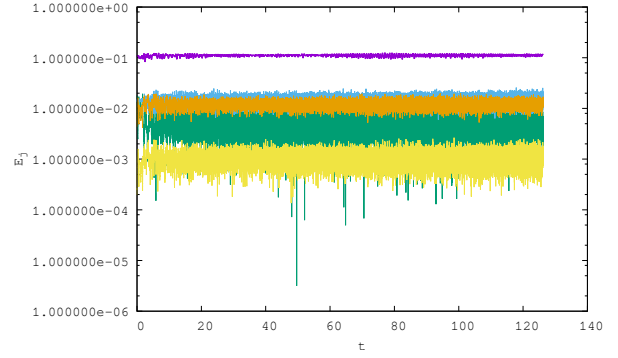


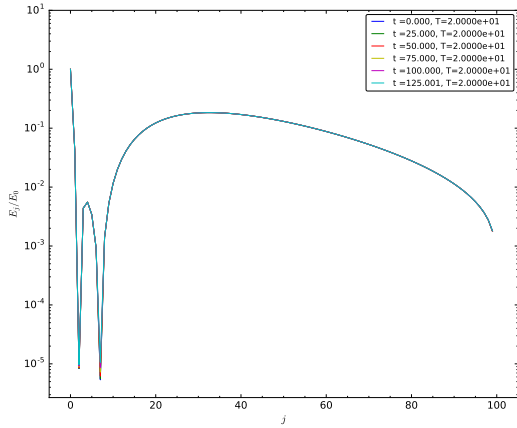
Figure 3.16: A high-temperature solution is padded with 25 extra modes, then evolved in time. Above are the results of projecting back to the QP plane at $t \simeq 0.002, 0.004, 0.006, 0.06$ (red diamond, green cross, blue square, yellow triangle, magenta circle).



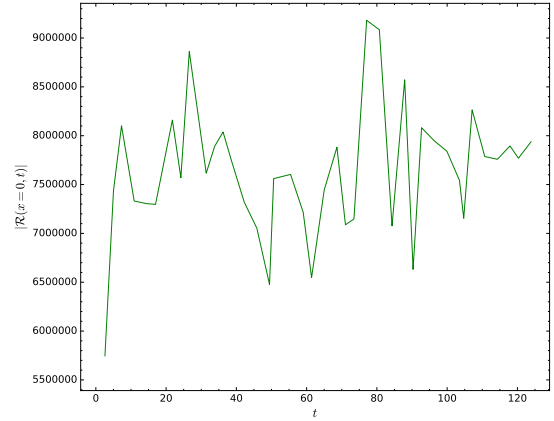
(a) *Evolution of the first four modes.*



(b) *Comparative evolution of modes $j = 0, 25, 50, 75, 99$.*



(c) *Energy spectrum at selected times throughout the evolution.*



(d) *The upper envelope of the Ricci scalar at the origin, per light-crossing time.*

Figure 3.17: *The evolution of an intermediate, high-temperature solution that does not correspond to a solution of the QP equations.*

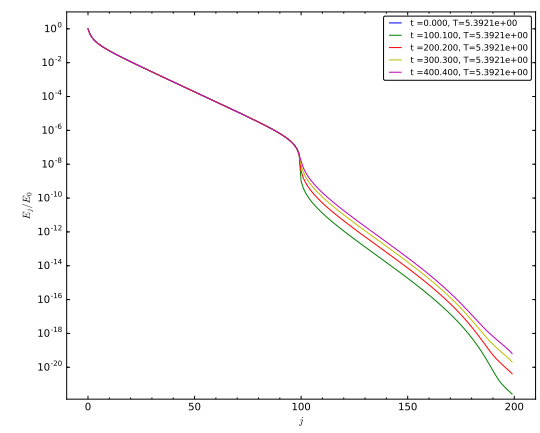
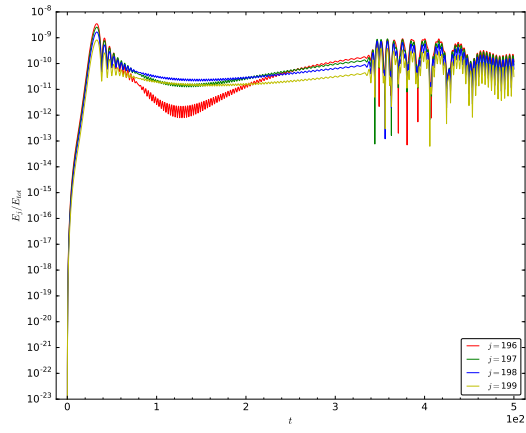
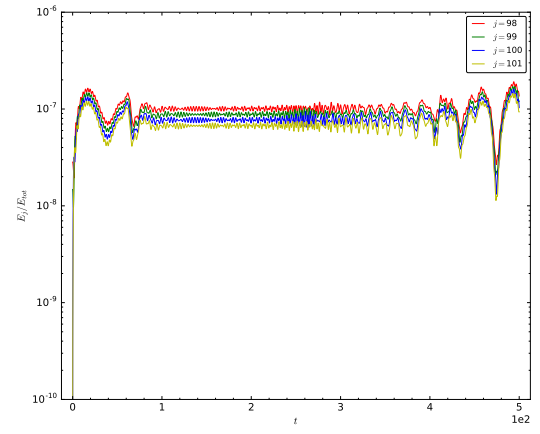
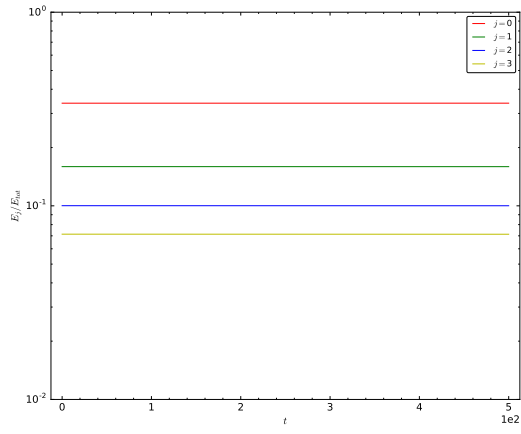
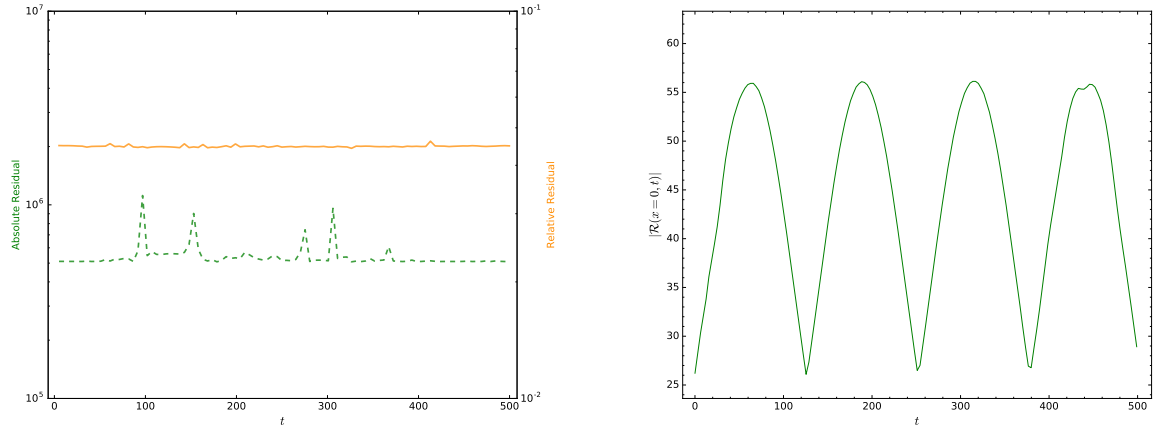


Figure 3.18: *Padding a threshold temperature solution*



(a) The residuals of (3.19) during the evolution of the padded threshold temperature solutions shown in figure 3.18.

(b) The upper envelope of the Ricci scalar at the origin per light-crossing time for the padded threshold temperature solution.

Figure 3.19: Despite the spectrum of the padded threshold temperature solution (figure 3.18) resembling that of lower-temperature QP solutions, these solutions move away from the QP plane and can no longer be projected back.

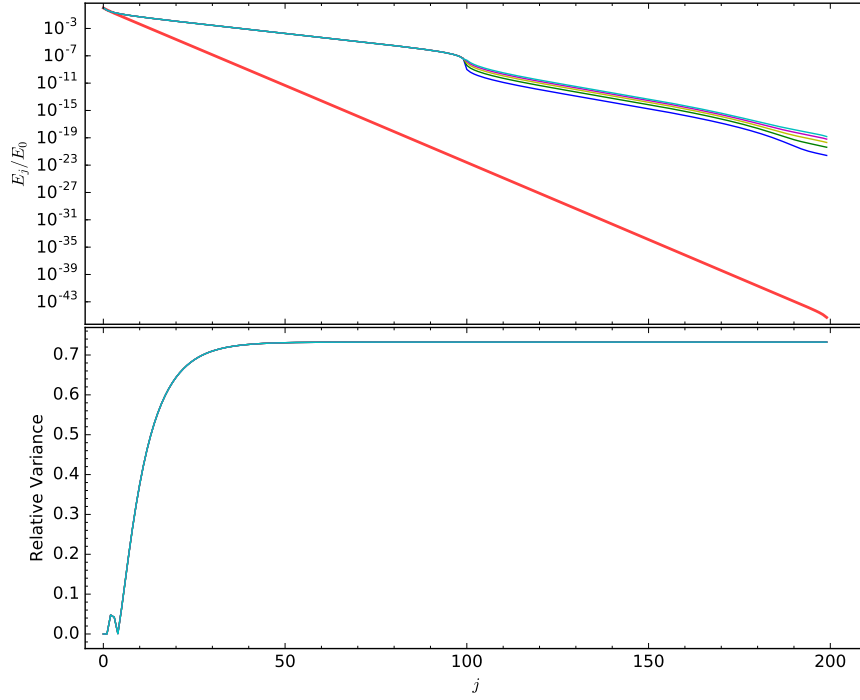


Figure 3.20: *Top: Overlay of the known threshold temperature solution for $j_{\max} = 200$ (thick red line) with snapshots of the spectra of a $j_{\max} = 100$ threshold solution that has been padded with zeros to $j_{\max} = 200$ after amplitude/phase evolutions of $\tau = 1, 2, 3, 4, 5 \times 10^{-5}$ (blue, green, yellow, magenta, cyan). Bottom: The absolute value of the difference between the cumulative sums of the $j_{\max} = 200$ threshold temperature solution and each snapshot spectrum (same colouring).*

Appendix

3.A Seeding Methods For Non-Linear Solvers

While it was originally proposed by [14] that the appropriate seed value for nonlinear solvers be given by the exponential relation ($j > 1$)

$$\alpha_j \sim \frac{3e^{-\mu j}}{2j + 3} \quad (3.27)$$

in AdS_4 , where $\mu = \ln(3/5\alpha_1)$, as j_{max} increased, the seed values diverged significantly from the true solutions (see figure 3.A.1 for a comparison between known QP solutions and the seeds generated by (3.27)). Although this profile was sufficient for low j_{max} solutions, above $j_{max} \gtrsim 150$, (3.27) no longer provided an adequate starting guess. To overcome this problem, exponential fitting was applied to the tail values of a known QP solution with lower j_{max} . Using this exponential fit, the data was extrapolated to a higher j_{max} .

Care was taken to avoid edge effects due to truncation when choosing the points that constituted the tail of the data. To illustrate the variance of the solution with truncation, we examine a fixed α_j value over a variety of j_{max} , starting with $\alpha_j = \alpha_{j_{max}}$. In table 3.A.1 we see that the value of α_{50} for QP solutions with $\alpha_1 = 0.2$ becomes impervious to truncation effects once $j_{max} > 55$.

To err on the side of caution, the modes $[j_{max} - 30, j_{max} - 10]$ were used from each QP solution to provide more accurate seed values for $j_{max} + 25$ solutions. See figure 3.A.2a for a comparison of seed values generated by tail fitting to actual QP solutions. The solutions found using this method of seeding versus those found from the seeding given in (3.27) had relative differences on the order of 10^{-14} (see figure 3.A.2b).

3.B Auxiliary Integrals For Calculating the T, R, S Coefficients

The auxiliary coefficients X, Y, W, W^*, A , and V allow the symmetries of the T, R and S coefficients to be more easily recognized and therefore reduce the number of total calculations involved in determining (3.34) - (3.36). These auxiliary coefficients are written simply in terms of the eigenfunctions

j_{max}	α_{50}
50	1.74597252e-26
51	1.82668391e-26
52	1.83346256e-26
53	1.83408260e-26
54	1.83414138e-26
55	1.83414706e-26
60	1.83414768e-26
65	1.83414768e-26
70	1.83414768e-26
75	1.83414768e-26

Table 3.A.1: α_{50} values for various j_{max} QP solutions.

in (3.9) and their derivatives. Explicitly, they are

$$X_{ijkl} = \int_0^{\pi/2} dx e'_i(x) e_j(x) e_k(x) e_l(x) \sin(x) \cos(x) (\tan(x))^{d-1} \quad (3.28)$$

$$Y_{ijkl} = \int_0^{\pi/2} dx e'_i(x) e_j(x) e'_k(x) e'_l(x) \sin(x) \cos(x) (\tan(x))^{d-1} \quad (3.29)$$

$$W_{ijkl} = \int_0^{\pi/2} dx e_i(x) e_j(x) \sin(x) \cos(x) \int_0^x dy e_k(y) e_l(y) (\tan(y))^{d-1} \quad (3.30)$$

$$W_{ijkl}^* = \int_0^{\pi/2} dx e'_i(x) e'_j(x) \sin(x) \cos(x) \int_0^x dy e_k(y) e_l(y) (\tan(y))^{d-1} \quad (3.31)$$

$$A_{ij} = \int_0^{\pi/2} dx e'_i(x) e'_j(x) \sin(x) \cos(x) \quad (3.32)$$

$$V_{ij} = \int_0^{\pi/2} dx e_i(x) e_j(x) \sin(x) \cos(x) . \quad (3.33)$$

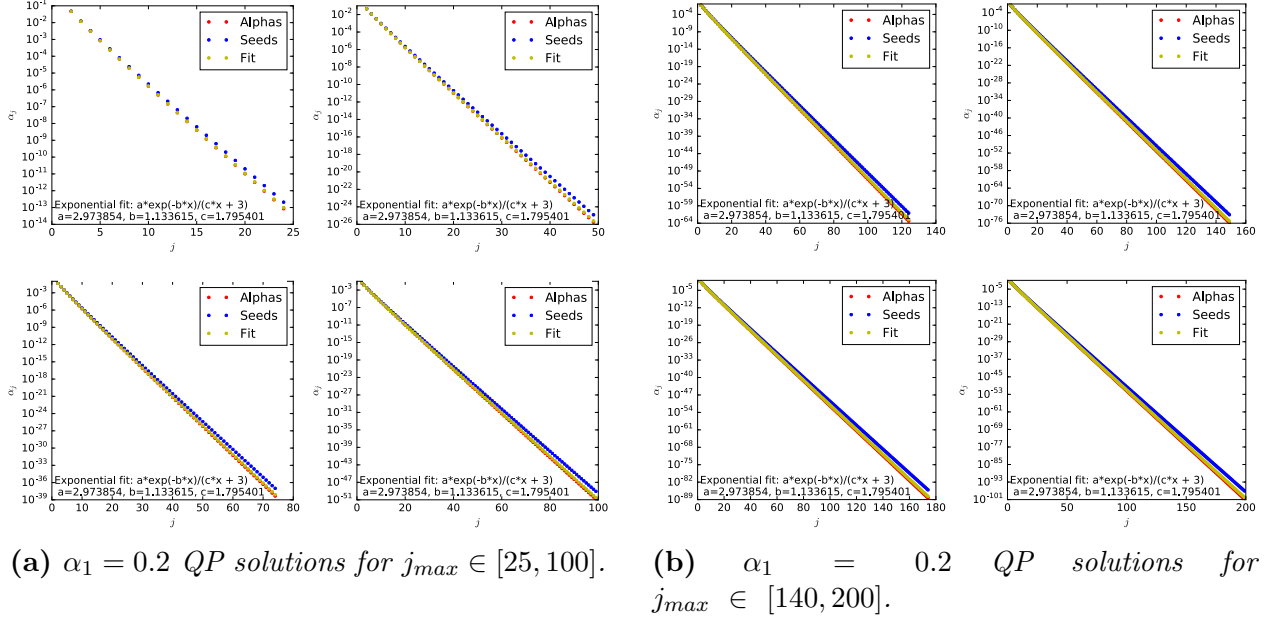


Figure 3.A.1: A comparison of seeds predicted by (3.27) to known QP solution. Also included for comparison are the results of fitting the QP solutions to a generic exponential fit.

In terms of these coefficients, the TTF source terms are given by

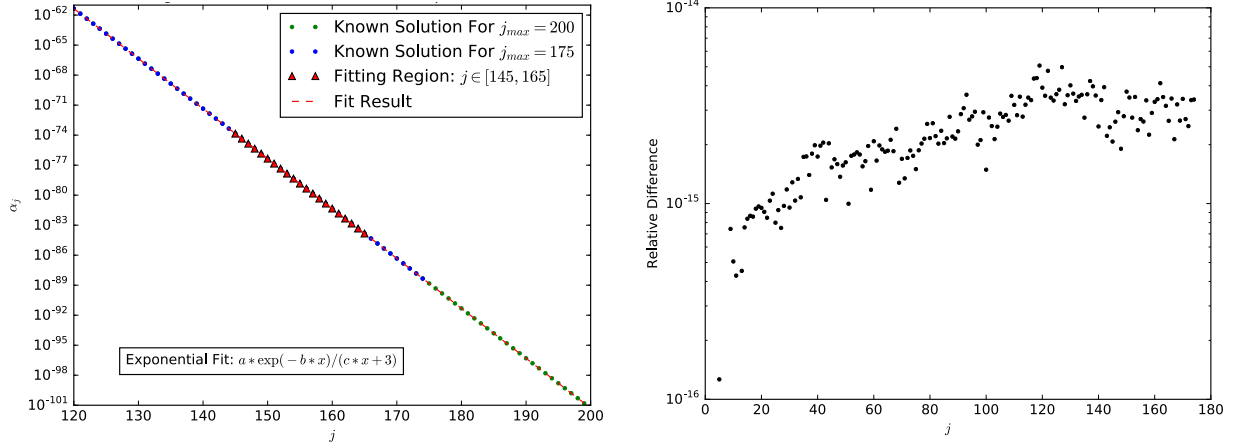
$$T_l = \frac{1}{2}\omega_l^2 X_{ull} + \frac{3}{2}Y_{ull} + 2\omega_l^4 W_{ull} + 2\omega_l^2 W_{ull}^* - \omega_l^2(A_{ul} + \omega_l^2 V_{ul}) \quad (3.34)$$

$$\begin{aligned} R_{il} = & \frac{1}{2} \left(\frac{\omega_i^2 + \omega_l^2}{\omega_l^2 - \omega_i^2} \right) (\omega_l^2 X_{illi} - \omega_i^2 X_{liil}) + 2 \left(\frac{\omega_l^2 Y_{ilil} - \omega_i^2 Y_{lili}}{\omega_l^2 - \omega_i^2} \right) \\ & + \left(\frac{\omega_i^2 \omega_l^2}{\omega_l^2 - \omega_i^2} \right) (X_{illi} - X_{lili}) + \frac{1}{2} (Y_{iill} + Y_{lili}) + \omega_i^2 \omega_l^2 (W_{liii} + W_{iill}) \\ & + \omega_i^2 W_{liii}^* + \omega_l^2 W_{iill}^* - \omega_l^2 (A_{ii} + \omega_i^2 V_{ii}) \end{aligned} \quad (3.35)$$

$$\begin{aligned} S_{ijkl} = & -\frac{1}{4} \left(\frac{1}{\omega_i + \omega_j} + \frac{1}{\omega_i - \omega_k} + \frac{1}{\omega_j - \omega_k} \right) (\omega_i \omega_j \omega_k X_{lijl} - \omega_l Y_{iljk}) \\ & - \frac{1}{4} \left(\frac{1}{\omega_i + \omega_j} + \frac{1}{\omega_i - \omega_k} - \frac{1}{\omega_j - \omega_k} \right) (\omega_j \omega_k \omega_l X_{ijkl} - \omega_i Y_{jikl}) \\ & - \frac{1}{4} \left(\frac{1}{\omega_i + \omega_j} - \frac{1}{\omega_i - \omega_k} + \frac{1}{\omega_j - \omega_k} \right) (\omega_i \omega_k \omega_l X_{jikl} - \omega_j Y_{ijkl}) \\ & - \frac{1}{4} \left(\frac{1}{\omega_i + \omega_j} - \frac{1}{\omega_i - \omega_k} - \frac{1}{\omega_j - \omega_k} \right) (\omega_i \omega_j \omega_l X_{kijl} - \omega_k Y_{ikjl}). \end{aligned} \quad (3.36)$$

3.C Frequency of Solution Checking

The frequency of applying the nonlinear solver to project back down to the QP solution plane is an important part of ensuring that the perturbative method remains applicable. If QP solutions are perturbed by too large an energy, or for too many iterations, the intermediate solutions may not be close enough to the solution plane to provide an adequate seed value. Such was the concern when



(a) Fitting the tail of the $j_{max} = 175$ spectrum to construct a seed for $j_{max} = 200$ at fixed $\alpha_1 = 0.2$. Also included is actual QP spectrum for $j_{max} = 200$. (b) Relative difference between $\alpha_1 = 0.2$ QP solutions found using tail-fitting and those from the exponential profile (3.27).

Figure 3.A.2: The process and result of tail fitting the α_j spectra of QP solutions to generate better seed values.

examining the purported high-temperature solutions from existing sources.

For example, consider the process of applying perturbations of $\delta E = 0.01\%$ up to some intermediate temperature without projecting back to the QP plane, then projecting back every 100 iterations until a maximum temperature is reached. Starting with the QP solution corresponding to $\alpha_1 = 0.2$, the lower panel of figure 3.C.1 shows the result of repeated perturbations of $\delta E = 0.01\%$ that are not projected back to the QP plane.

The behaviour of the spectra differ for the low and high j_{max} cases. For the $j_{max} = 50$ solutions, the spectra in the lower panel of the figure can remain smooth through more than 27,000 iterations of δE perturbations. When a temperature of approximately 17 is reached, the spectrum is used as a seed value for the nonlinear solver and a smooth solution is found. Continuing with the same δE , but reapplying the nonlinear solver produces mixed results; the temperatures of increasing iterations do not increase monotonically, but do always project back to a solution with nearly the same temperature. However, the spectra themselves develop kinks by iteration 3,100 that are indicative of a change of sign in the alpha values and a breakdown of the perturbative condition. Because only a small number of modes are considered, numerical solutions are still found by the Newton-Raphson solver but no longer represent physical states. Continuing this procedure, we find that the solver fails to find a solution even at the modest temperature of $T \simeq 38$.

The behaviour of the $j_{max} = 150$ solutions is consistent with their lower-mode number counterparts, albeit more pronounced. We see that kinks in the spectrum develop even when the nonlinear solver has not been applied. The intermediate solution used as a seed for the nonlinear solver did not project back to a nearby temperature, instead falling from $T \simeq 14.2$ to $T \simeq 4.3$. As the perturbative procedure continued, projection back to the QP plane was only possible in for a short time before no solution could be found. Note the numerous spikes in the energy spectrum shown in the upper panel. For $j_{max} = 150$, we conclude that no physically relevant high-temperature solutions exist, even as low as $T \simeq 4.76$.

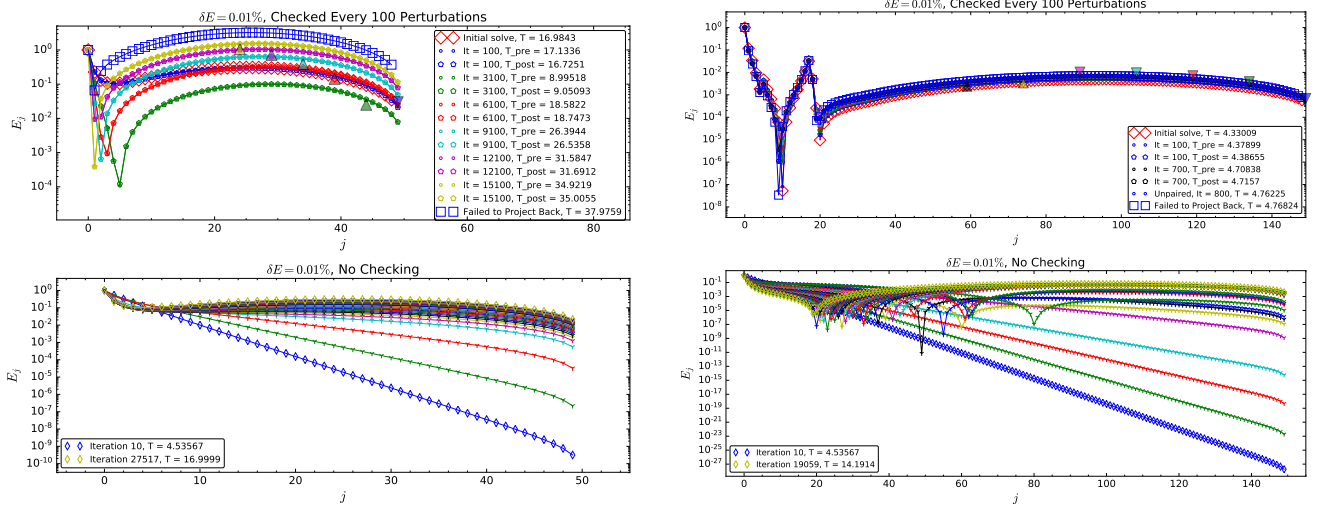


Figure 3.C.1: Left: the result of unchecked perturbations of a $j_{\max} = 50$ QP solution up to an intermediate temperature before switching to regular checking. Right: the same procedure is applied to a $j_{\max} = 150$ QP solution.

4 Driven, Time-Dependent Operators in Conformal Field Theories

Will be published to the arXiv, then submitted to JHEP

4.1 Contributions

All contributions are mine.

Driven TTF

To Appear on arxiv.org

Brad Cownden¹

¹*Department of Physics & Astronomy,
University of Manitoba
Winnipeg, Manitoba R3T 2N2, Canada
cowndenb@myumanitoba.ca*

Abstract

4.2 Introduction

4.3 Massive Scalars in AdS_{d+1}

4.4 Discussion

Acknowledgments The work of BC and AF is supported by the Natural Sciences and Engineering Research Council of Canada Discovery Grant program. This research was enabled in part by support provided by WestGrid (www.westgrid.ca) and Compute Canada Calcul Canada (www.computecanada.ca).

Appendix

4.A An Appendix

Bibliography

- [1] P. Bizon and A. Rostworowski, *On weakly turbulent instability of anti-de Sitter space*, *Phys. Rev. Lett.* **107** (2011) 031102, [[1104.3702](#)].
- [2] D. Garfinkle and L. A. Pando Zayas, *Rapid Thermalization in Field Theory from Gravitational Collapse*, *Phys. Rev.* **D84** (2011) 066006, [[1106.2339](#)].
- [3] J. Jalmuzna, A. Rostworowski and P. Bizon, *A Comment on AdS collapse of a scalar field in higher dimensions*, *Phys. Rev.* **D84** (2011) 085021, [[1108.4539](#)].
- [4] D. Garfinkle, L. A. Pando Zayas and D. Reichmann, *On Field Theory Thermalization from Gravitational Collapse*, *JHEP* **02** (2012) 119, [[1110.5823](#)].
- [5] O. J. C. Dias, G. T. Horowitz and J. E. Santos, *Gravitational Turbulent Instability of Anti-de Sitter Space*, *Class. Quant. Grav.* **29** (2012) 194002, [[1109.1825](#)].
- [6] V. Balasubramanian, A. Buchel, S. R. Green, L. Lehner and S. L. Liebling, *Holographic Thermalization, Stability of Anti-de Sitter Space, and the Fermi-Pasta-Ulam Paradox*, *Phys. Rev. Lett.* **113** (2014) 071601, [[1403.6471](#)].
- [7] B. Craps, O. Evnin and J. Vanhoof, *Renormalization group, secular term resummation and AdS (in)stability*, *JHEP* **10** (2014) 048, [[1407.6273](#)].
- [8] P. Basu, C. Krishnan and A. Saurabh, *A stochasticity threshold in holography and the instability of AdS*, *Int. J. Mod. Phys.* **A30** (2015) 1550128, [[1408.0624](#)].
- [9] F. V. Dimitrakopoulos, B. Freivogel, M. Lippert and I.-S. Yang, *Position space analysis of the AdS (in)stability problem*, *JHEP* **08** (2015) 077, [[1410.1880](#)].
- [10] A. Buchel, S. R. Green, L. Lehner and S. L. Liebling, *Conserved quantities and dual turbulent cascades in anti-de Sitter spacetime*, *Phys. Rev.* **D91** (2015) 064026, [[1412.4761](#)].
- [11] B. Craps, O. Evnin and J. Vanhoof, *Renormalization, averaging, conservation laws and AdS (in)stability*, *JHEP* **01** (2015) 108, [[1412.3249](#)].
- [12] O. Evnin and C. Krishnan, *A Hidden Symmetry of AdS Resonances*, *Phys. Rev.* **D91** (2015) 126010, [[1502.03749](#)].
- [13] F. Dimitrakopoulos and I.-S. Yang, *Conditionally extended validity of perturbation theory: Persistence of AdS stability islands*, *Phys. Rev.* **D92** (2015) 083013, [[1507.02684](#)].
- [14] S. R. Green, A. Maillard, L. Lehner and S. L. Liebling, *Islands of stability and recurrence times in AdS*, *Phys. Rev.* **D92** (2015) 084001, [[1507.08261](#)].

- [15] B. Craps, O. Evnin and J. Vanhoof, *Ultraviolet asymptotics and singular dynamics of AdS perturbations*, *JHEP* **10** (2015) 079, [[1508.04943](#)].
- [16] B. Craps, O. Evnin, P. Jai-akson and J. Vanhoof, *Ultraviolet asymptotics for quasiperiodic AdS_4 perturbations*, *JHEP* **10** (2015) 080, [[1508.05474](#)].
- [17] B. Craps and O. Evnin, *AdS (in)stability: an analytic approach*, *Fortsch. Phys.* **64** (2016) 336–344, [[1510.07836](#)].
- [18] A. Buchel, S. L. Liebling and L. Lehner, *Boson stars in AdS spacetime*, *Phys. Rev.* **D87** (2013) 123006, [[1304.4166](#)].
- [19] M. Maliborski and A. Rostworowski, *A comment on "Boson stars in AdS"*, [1307.2875](#).
- [20] M. Maliborski and A. Rostworowski, *Lecture Notes on Turbulent Instability of Anti-de Sitter Spacetime*, *Int. J. Mod. Phys. A* **28** (2013) 1340020, [[1308.1235](#)].
- [21] P. Bizoń and A. Rostworowski, *Comment on "Holographic Thermalization, Stability of Anti-de Sitter Space, and the Fermi-Pasta-Ulam Paradox"*, *Phys. Rev. Lett.* **115** (2015) 049101, [[1410.2631](#)].
- [22] V. Balasubramanian, A. Buchel, S. R. Green, L. Lehner and S. L. Liebling, *Reply to Comment on "Holographic Thermalization, Stability of Anti-de Sitter Space, and the Fermi-Pasta-Ulam Paradox"*, *Phys. Rev. Lett.* **115** (2015) 049102, [[1506.07907](#)].
- [23] P. Bizoń, M. Maliborski and A. Rostworowski, *Resonant Dynamics and the Instability of Anti-de Sitter Spacetime*, *Phys. Rev. Lett.* **115** (2015) 081103, [[1506.03519](#)].
- [24] N. Deppe, *On the stability of anti-de Sitter spacetime*, [1606.02712](#).
- [25] F. V. Dimitrakopoulos, B. Freivogel, J. F. Pedraza and I.-S. Yang, *Gauge dependence of the AdS instability problem*, *Phys. Rev.* **D94** (2016) 124008, [[1607.08094](#)].
- [26] F. V. Dimitrakopoulos, B. Freivogel and J. F. Pedraza, *Fast and Slow Coherent Cascades in Anti-de Sitter Spacetime*, *Class. Quant. Grav.* **35** (2018) 125008, [[1612.04758](#)].
- [27] S. L. Liebling and G. Khanna, *Scalar collapse in AdS with an OpenCL open source code*, *Class. Quant. Grav.* **34** (2017) 205012, [[1706.07413](#)].
- [28] P. Bizoń and J. Jałmużna, *Globally regular instability of AdS_3* , *Phys. Rev. Lett.* **111** (2013) 041102, [[1306.0317](#)].
- [29] E. da Silva, E. Lopez, J. Mas and A. Serantes, *Collapse and Revival in Holographic Quenches*, *JHEP* **04** (2015) 038, [[1412.6002](#)].
- [30] N. Deppe, A. Kolly, A. R. Frey and G. Kunstatter, *Black Hole Formation in AdS Einstein-Gauss-Bonnet Gravity*, *JHEP* **10** (2016) 087, [[1608.05402](#)].
- [31] N. Deppe, A. Kolly, A. Frey and G. Kunstatter, *Stability of AdS in Einstein Gauss Bonnet Gravity*, *Phys. Rev. Lett.* **114** (2015) 071102, [[1410.1869](#)].

- [32] R. Arias, J. Mas and A. Serantes, *Stability of charged global AdS_4 spacetimes*, *JHEP* **09** (2016) 024, [[1606.00830](#)].
- [33] H. Okawa, J. C. Lopes and V. Cardoso, *Collapse of massive fields in anti-de Sitter spacetime*, [1504.05203](#).
- [34] N. Deppe and A. R. Frey, *Classes of Stable Initial Data for Massless and Massive Scalars in Anti-de Sitter Spacetime*, *JHEP* **12** (2015) 004, [[1508.02709](#)].
- [35] V. E. Hubeny and M. Rangamani, *Unstable horizons*, *JHEP* **05** (2002) 027, [[hep-th/0202189](#)].
- [36] A. Buchel and L. Lehner, *Small black holes in $AdS_5 \times S^5$* , *Class. Quant. Grav.* **32** (2015) 145003, [[1502.01574](#)].
- [37] A. Buchel, *Universality of small black hole instability in AdS/CFT* , *Int. J. Mod. Phys. D* **26** (2017) 1750140, [[1509.07780](#)].
- [38] A. Buchel and M. Buchel, *On stability of nonthermal states in strongly coupled gauge theories*, [1509.00774](#).
- [39] R. Brito, V. Cardoso and J. V. Rocha, *Interacting shells in AdS spacetime and chaos*, *Phys. Rev. D* **94** (2016) 024003, [[1602.03535](#)].
- [40] O. Aharony, S. S. Gubser, J. M. Maldacena, H. Ooguri and Y. Oz, *Large N field theories, string theory and gravity*, *Phys. Rept.* **323** (2000) 183–386, [[hep-th/9905111](#)].
- [41] H. Nastase, *Introduction to the ADS/CFT Correspondence*. Cambridge University Press, 2015.
- [42] P. R. Brady, C. M. Chambers and S. M. C. V. Goncalves, *Phases of massive scalar field collapse*, *Phys. Rev. D* **56** (1997) 6057–6061, [[gr-qc/9709014](#)].
- [43] D. Santos-Oliván and C. F. Sopuerta, *Moving closer to the collapse of a massless scalar field in spherically symmetric anti-de Sitter spacetimes*, *Phys. Rev. D* **93** (2016) 104002, [[1603.03613](#)].
- [44] G. Martinon, *The instability of anti-de Sitter space-time*, [1708.05600](#).
- [45] A. Buchel, L. Lehner and S. L. Liebling, *Scalar Collapse in AdS* , *Phys. Rev. D* **86** (2012) 123011, [[1210.0890](#)].
- [46] J. Jałmużna, C. Gundlach and T. Chmaj, *Scalar field critical collapse in 2+1 dimensions*, *Phys. Rev. D* **92** (2015) 124044, [[1510.02592](#)].
- [47] P. Bizoń, *Is AdS stable?*, *Gen. Rel. Grav.* **46** (2014) 1724, [[1312.5544](#)].
- [48] M. Maliborski and A. Rostworowski, *Time-Periodic Solutions in an Einstein AdS -Massless-Scalar-Field System*, *Phys. Rev. Lett.* **111** (2013) 051102, [[1303.3186](#)].
- [49] M. Maliborski and A. Rostworowski, *What drives AdS spacetime unstable?*, *Phys. Rev. D* **89** (2014) 124006, [[1403.5434](#)].

- [50] G. Fodor, P. Forgács and P. Grandclément, *Self-gravitating scalar breathers with negative cosmological constant*, *Phys. Rev.* **D92** (2015) 025036, [[1503.07746](#)].
- [51] O. J. C. Dias, G. T. Horowitz, D. Marolf and J. E. Santos, *On the Nonlinear Stability of Asymptotically Anti-de Sitter Solutions*, *Class. Quant. Grav.* **29** (2012) 235019, [[1208.5772](#)].
- [52] B. Cownden, N. Deppe and A. R. Frey, *Phase Diagram of Stability for Massive Scalars in Anti-de Sitter Spacetime*, [1711.00454](#).
- [53] R. Brito, V. Cardoso and J. V. Rocha, *Interacting shells in AdS spacetime and chaos*, *Phys. Rev.* **D94** (2016) 024003, [[1602.03535](#)].
- [54] O. Dias and J. E. Santos, *AdS nonlinear instability: moving beyond spherical symmetry*, *Class. Quant. Grav.* **33** (2016) 23LT01, [[1602.03890](#)].
- [55] O. J. C. Dias and J. E. Santos, *AdS nonlinear instability: breaking spherical and axial symmetries*, [1705.03065](#).
- [56] M. W. Choptuik, O. J. C. Dias, J. E. Santos and B. Way, *Collapse and Nonlinear Instability of AdS Space with Angular Momentum*, *Phys. Rev. Lett.* **119** (2017) 191104, [[1706.06101](#)].